



UNIVERSITY OF LEEDS

This is a repository copy of *Substitution of Ti³⁺ and Ti⁴⁺ in hibonite (CaAl₁₂O₁₉)*.

White Rose Research Online URL for this paper:

<http://eprints.whiterose.ac.uk/79652/>

Version: Accepted Version

Article:

Doyle, PM, Schofield, PF, Berry, AF et al. (2 more authors) (2014) Substitution of Ti³⁺ and Ti⁴⁺ in hibonite (CaAl₁₂O₁₉). *American Mineralogist: an international journal of earth and planetary materials*, 99 (7). 1369 - 1382 (14). ISSN 0003-004X

<https://doi.org/10.2138/am.2014.4532>

Reuse

Unless indicated otherwise, fulltext items are protected by copyright with all rights reserved. The copyright exception in section 29 of the Copyright, Designs and Patents Act 1988 allows the making of a single copy solely for the purpose of non-commercial research or private study within the limits of fair dealing. The publisher or other rights-holder may allow further reproduction and re-use of this version - refer to the White Rose Research Online record for this item. Where records identify the publisher as the copyright holder, users can verify any specific terms of use on the publisher's website.

Takedown

If you consider content in White Rose Research Online to be in breach of UK law, please notify us by emailing eprints@whiterose.ac.uk including the URL of the record and the reason for the withdrawal request.



eprints@whiterose.ac.uk
<https://eprints.whiterose.ac.uk/>

1 **Revision 2**

2 **Substitution of Ti³⁺ and Ti⁴⁺ in hibonite (CaAl₂O₁₉)**

3
4 Patricia M. Doyle^{1,2,†}, Paul F. Schofield², Andrew J. Berry^{1,2,*}, Andrew M. Walker^{3‡} and Kevin S.
5 Knight^{4,2}

6
7 ¹ Department of Earth Science and Engineering, Imperial College London, South Kensington. SW7
8 2AZ. UK

9 ² Department of Earth Sciences, Natural History Museum, Cromwell Road, London. SW7 5BD. UK

10 ³ School of Earth Sciences, University of Bristol, Wills Memorial Building, Queen's Road, Bristol.
11 BS8 1RJ. UK

12 ⁴ ISIS Science Division, Rutherford Appleton Laboratory, Chilton, Didcot. OX11 0QX. UK

13
14
15 [†] Present address: Hawai'i Institute of Geophysics and Planetology, University of Hawai'i at
16 Manoa, 96822, USA

17 ^{*} Present address: Research School of Earth Sciences, Australian National University, Canberra,
18 ACT, 2601 Australia

19 [‡] Present address: School of Earth and Environment, University of Leeds, Leeds, LS2 9JT, UK

20
21
22 **Abstract**

23 The structures of eight synthetic samples of hibonite, with variable Ti oxidation state and Ti
24 concentrations (2.4-15.9 wt% TiO₂) that span the range reported for natural hibonite found in
25 meteorites, were determined by Rietveld refinements of neutron powder diffraction data. Ti³⁺ was
26 found to exclusively occupy the octahedral face-sharing M4 site irrespective of the presence or
27 absence of Ti⁴⁺. Ti⁴⁺ partitions between the trigonal bipyramidal M2 site and the M4 site. The ratio
28 (Ti⁴⁺ on M2):(Ti⁴⁺ on M4) appears to be constant for all the samples, with an average of 0.18(2)
29 irrespective of the concentrations of Ti³⁺ and Ti⁴⁺. These substitutional sites were shown to be the
30 most stable configurations for Ti in hibonite from calculations using density functional theory,
31 although the predicted preference of Ti⁴⁺ for M4 over M2 is not as strong as is observed. This is
32 attributed to the different Ti contents of the experimental and calculated structures and suggests that
33 the Ti site occupancies might change between these concentrations. Furthermore, it is shown that
34 Ti has a preference to occupy neighbouring M4 sites such that Ti-Ti interactions occur with
35 stabilization energies of 83 kJ/mol for Ti³⁺-Ti³⁺ and at least 15 kJ/mol for Ti⁴⁺-Ti⁴⁺. Features in
36 optical spectroscopy and electron spin resonance data from meteoritic and synthetic hibonites that

37 have been used to infer Ti^{3+}/Ti^{4+} are shown to actually derive from these Ti-Ti interactions. The
38 amount of Ti^{4+} in hibonite can be determined from the unit-cell parameters if ΣTi is determined
39 independently. Ti^{3+}/Ti^{4+} in hibonite may record the oxygen fugacity (f_{O_2}) of the early solar nebula,
40 however, the existence of $Ti^{3+}-Ti^{3+}$ and $Ti^{4+}-Ti^{4+}$ interactions and the potential for $Ti^{4+}-Ti^{3+}$
41 interactions need to be considered when interpreting spectroscopic data in terms of Ti valence state
42 and f_{O_2} . Hibonite as a single-mineral oxybarometer must be used with caution due to the potential
43 role of crystal chemistry (including Ti-Ti interactions) to stabilise Ti oxidation states independently
44 of f_{O_2} .

45

46

47

48 Keywords: hibonite, titanium substitution, site occupancy, CAI, neutron diffraction, density
49 functional theory, oxygen fugacity

50

Introduction

51 Some of the oldest materials in the Solar System are the refractory calcium-aluminium-rich
52 inclusions (CAIs) found in undifferentiated chondritic meteorites (Amelin et al. 2002). Hibonite
53 ($\text{CaAl}_{12}\text{O}_{19}$), a mineral found within some CAIs, is thought to be the second major phase to
54 condense from a gas of solar composition (Lodders 2003). Moreover, hibonite is the first mineral
55 to condense that can incorporate significant amounts of polyvalent elements such as Ti, V, Cr and
56 Fe into its structure. As a result, hibonite has the potential to record the conditions present in the
57 early Solar System, in particular the composition and hence oxygen fugacity (f_{O_2}) of the nebular
58 gas. For terrestrial materials the intrinsic f_{O_2} is usually determined from $\text{Fe}^{2+}/\text{Fe}^{3+}$, however, this is
59 impractical for CAIs as the extremely reducing conditions of formation usually result in the
60 presence of metallic Fe (i.e. $\text{Fe}^0/\text{Fe}^{2+}$). The most suitable alternative redox sensor is $\text{Ti}^{3+}/\text{Ti}^{4+}$ (e.g.
61 Grossman et al. 2008) since Ti is a significant component of CAIs and the ratio varies over the
62 range of expected f_{O_2} s (Simon et al. 2007). Meteoritic hibonite may contain up to ~ 8 wt% TiO_2
63 (Allen et al. 1978) and consequently has the potential to be utilised as a single-mineral
64 oxybarometer.

65

66 Hibonite crystals in CAIs can be colourless, greenish-blue, blue or orange and these
67 differences have been used to infer variations in the oxidation state of Ti, and to a lesser degree V
68 (e.g. Burns and Burns 1984; Ihinger and Stolper 1986); such colour changes have even been
69 reported to occur between the core and rim of individual hibonite crystals (Rout and Bischoff
70 2008). Previous studies of meteoritic hibonite by optical absorption spectroscopy and electron spin
71 resonance (ESR) spectroscopy (Ihinger and Stolper 1986; Beckett et al. 1988) have confirmed the
72 presence of Ti^{3+} and suggested $\text{Ti}^{3+}/\Sigma\text{Ti}$ (where $\Sigma\text{Ti} = \text{Ti}^{3+} + \text{Ti}^{4+}$) values up to 0.2. However,
73 accurate measurement of $\text{Ti}^{3+}/\text{Ti}^{4+}$ in materials is not necessarily a simple process. The
74 determination of $\text{Ti}^{3+}/\text{Ti}^{4+}$ from stoichiometry or wet chemistry is notoriously problematic (e.g.
75 Beckett et al. 1988; Rager et al. 2003), while both optical and ESR spectroscopies are impeded by
76 the presence of Fe, which is ubiquitous in natural systems. Further, the size and inhomogeneity of
77 meteoritic hibonite crystals generally require the use of microbeam techniques. X-ray absorption
78 near edge structure (XANES) spectroscopy and X-ray photo emission electron microscopy
79 (XPEEM) have the potential to non-destructively quantify valence states, including $\text{Ti}^{3+}/\Sigma\text{Ti}$, with
80 micron (e.g. Berry et al. 2008; Simon et al. 2007) and sub-micron (e.g. Smith et al. 2004; Schofield
81 et al. 2010) spatial resolution, respectively.

82

83 The spectroscopic quantification of $\text{Ti}^{3+}/\Sigma\text{Ti}$ is strongly dependent on the interpretation of

84 spectra from suitable standards. Spectral detail is in turn directly related to the crystal chemistry of
85 the phase in question. Hibonite is crystal chemically complex, having five Al sites onto which Ti
86 may substitute and the preferred site occupancy of Ti is likely to be influenced by its oxidation
87 state. As yet there is no unambiguous description of the structural incorporation of Ti^{3+} and Ti^{4+}
88 into hibonite. We have used neutron powder diffraction (NPD) to structurally characterise a suite of
89 eight synthetic Ti-bearing hibonite samples, where $Ti^{3+}/\Sigma Ti$ varies between 0 and 1. As with X-ray
90 diffraction (XRD), NPD offers excellent contrast between Al and Ti, however, unlike XRD, NPD
91 also provides good contrast between Mg and Al and the fractional coordinates and atomic
92 displacement parameters of the oxygen atoms can be determined with high precision, thereby
93 increasing the certainty of the structural model. The findings of the NPD study are compared to,
94 and supported by, density functional theory (DFT) modelling.

95

96

Crystal Structure

97 The structure of hibonite ($CaAl_{12}O_{19}$) was first characterised by Curien et al. (1956) and
98 subsequently refined in a number of XRD studies (Kato and Saalfeld 1968; Utsunomiya et al. 1988;
99 Bermanec et al. 1996; Hofmeister et al. 2004; Nagashima et al. 2010). Hibonite is hexagonal (space
100 group $P63/mmc$, $Z=2$, $a \sim 5.6 \text{ \AA}$ and $c \sim 22.0 \text{ \AA}$; Hofmeister et al. 2004) and exhibits the
101 magnetoplumbite structure-type (Kato and Saalfeld 1968). The hibonite structure (Figure 1) is
102 dominated by polyhedral layers perpendicular to the c -axis, in which Ca occupies a 12-coordinated
103 polyhedron, and Al is distributed over five M sites. M1 is a regular octahedron (D_{3d}), M2 is a
104 trigonal bipyramid with an ideal site symmetry of D_{3h} , M3 is a tetrahedron (C_{3v}), M4 is a trigonally
105 distorted octahedron (C_{3v}) and M5 is a strongly distorted octahedron (C_s). The trigonal bipyramidal
106 site is split into two symmetrically-equivalent half-occupied sites above and below the equatorial
107 plane of the bipyramid by the static displacement of the M2 cation from the site-centre (Utsunomiya
108 et al. 1988; Du and Stebbins 2004). Within these pseudotetrahedral M2 sites the cation positions
109 are separated by 0.17-0.27 \AA (Bermanec et al. 1996; Hofmeister et al. 2004). The multiplicity of
110 the cation sites and their coordination numbers may be summarised as follows:

111 $^{[12]}Ca^{[6]}M1^{[5]}M2^{[4]}M3_2^{[6]}M4_2^{[6]}M5_6O_{19}$ (where coordination numbers are superscripted in square
112 brackets and the multiplicity of the site is subscripted).

113

114 The arrangement and distribution of the polyhedra in hibonite are such that the structural
115 topology can be considered in terms of a repetition of two distinct polyhedral layers perpendicular
116 to the c -axis (Burns and Burns, 1984; Nagashima et al. 2010). Within one of these layers, referred
117 to as the S-block, the tetrahedral (M3) and octahedral (M1 and M5) polyhedra are arranged as in the
118 spinel structure (Figure 1). These S-blocks are separated by a layer comprising the Ca site, the

119 trigonal bipyramidal M2 site and the octahedral M4 site, referred to as the R-block (Kohn and
120 Eckart 1964) or conductor layer (Iyi et al. 1989). The thickness of the R-block (along z) equates to
121 the O1-O1 distance between the apical oxygen atoms of the M2 site. The M2 polyhedra are
122 isolated from each other and linked by the M4 and Ca polyhedra. The M4 octahedra share a face,
123 forming isolated face-sharing pairs in which the M4 cations are separated by about 2.59 Å, parallel
124 to z (Hofmeister et al. 2004). The hibonite unit cell is formed by stacking R- and S-blocks along z
125 according to the sequence RSR'S', where R' and S' are rotated 180° about z relative to R and S
126 respectively (Bermanec et al. 1996).

127

128

Site Substitutions

129 A range of elements substitute into the hibonite structure (Table 1), with natural hibonites
130 containing Mg²⁺, Zn²⁺, Fe²⁺, Fe³⁺, Cr³⁺, V³⁺, Ti³⁺, Ti⁴⁺, Si⁴⁺ and Th⁴⁺ as major elements and the rare
131 earth elements La, Ce and Nd, at levels above 1000 ppm (e.g. Burns and Burns 1984; Beckett et al.
132 1988; Rakotondrazafy et al. 1996). Of particular interest to this study is Ti: Ti³⁺ may substitute
133 directly for Al³⁺, whereas Ti⁴⁺ undergoes a coupled substitution with Mg²⁺ for two Al³⁺ (Mg²⁺ +
134 Ti⁴⁺ ↔ 2Al³⁺) in order to maintain charge balance (Allen et al. 1978). Ti³⁺ is thought to occupy the
135 M2 site in hibonite based on crystal field stabilisation theory, and ESR and optical spectroscopies
136 (Burns and Burns, 1984; Beckett et al. 1988). In single crystal XRD studies of terrestrial hibonite,
137 Ti⁴⁺ has been reported to occupy only the M4 site (Bermanec et al. 1996) and both the M2 and the
138 M4 sites (Nagashima et al. 2010). The site occupancies of various elements in hibonite and
139 structural analogues, including natural and synthetic members of the magnetoplumbite group
140 (AB₁₂O₁₉) and β-alumina phases, are summarised in Table 1, indicating a large range of possible
141 sites for Ti³⁺ (M1, M2, M5) and Ti⁴⁺ (M1, M2, M4, M5).

142

143

Experimental

144 Synthesis

145 A suite of eight Ti-bearing hibonite samples was synthesized, two Ti³⁺ end-member samples
146 with Ti³⁺/ΣTi = 1, two Ti⁴⁺ end-member samples with Ti⁴⁺/ΣTi = 1 and four mixed-valent samples
147 with Ti³⁺/ΣTi between 0 and 1. All samples were synthesised at ~1400 °C, which is within the
148 stability field of hibonite in a gas of nebular composition (Yoneda and Grossman 1995) and well
149 below the experimentally determined incongruent melting temperature (1850 ± 10 °C in the CaO-
150 MgO-Al₂O₃ ± SiO₂ system; De Aza et al. 2000; Vázquez et al. 2003).

151

152 Stoichiometric mixtures of pre-dried CaCO₃, Al₂O₃, TiO₂ and MgO were pressed into pellets
153 and heated at ~1400 °C for ~30 h in graphite and an atmosphere of CO (logf_{O₂} = -16) for the Ti³⁺

154 end-member and mixed-valent samples and in Pt and CO₂ (log*f*_{O₂} = -3) for the Ti⁴⁺ end-member
155 samples. The synthesis of the mixed-valent samples relied on stoichiometry to control Ti³⁺/ΣTi
156 (noting the coupled substitution of Ti⁴⁺ and Mg²⁺) at constant *f*_{O₂}. All samples were cooled from
157 1400 to 600 °C over ~2 h. The Ti³⁺ end-member samples were essentially single phase after a
158 single sinter whereas the yield of Ti⁴⁺ hibonites was improved by a second sinter. At least 5 g of
159 each sample was prepared by combining the products of multiple individual experiments that were
160 sufficiently similar based upon XRD (Schofield et al. 2002). The chemical formulae of these Ti-
161 bearing hibonites and identities of any secondary phases identified are given in Table 2. The Ti³⁺
162 end-member and mixed-valent samples were all blue whereas the Ti⁴⁺ end-member samples were
163 white.

164

165 Throughout this manuscript the samples are identified by reference to their Ti per formula
166 unit (pfu) and Ti³⁺/ΣTi ratios in the form (Ti pfu, Ti³⁺/ΣTi). For example, the sample (0.5,1.0) will
167 have 0.5 Ti pfu and all the Ti will be Ti³⁺ giving a chemical formula of CaAl_{11.5}Ti_{0.5}O₁₉. The
168 sample (1.0,0) will have 1.0 Ti⁴⁺ pfu (and 1.0 Mg²⁺ pfu) giving a chemical formula of
169 CaAl_{10.0}Ti_{1.0}Mg_{1.0}O₁₉.

170

171 Scanning electron microscopy

172 Sintered samples were mounted in epoxy resin and the composition determined by energy
173 dispersive spectrometry using a Jeol 5900LV EDS SEM operated at 10 kV and 2 nA. The
174 fluorescence was calibrated to the K-lines of Ca in CaSiO₃, Al in Al₂O₃, Ti in TiO₂ rutile and Mg
175 and Si in Mg_{1.6}Fe_{0.4}SiO₄. Matrix corrections were made using the XPP routine (Oxford
176 Instruments).

177

178 Neutron powder diffraction

179 Neutron time-of-flight powder diffraction data were collected on the fixed geometry, high
180 resolution diffractometer HRPD (Ibberson et al. 1992) at the ISIS neutron spallation source,
181 Rutherford Appleton Laboratory, U.K. Between 2.8 and 4.4 g of sample were packed into an In
182 sealed cylindrical V can with an external diameter of 11 mm, and loaded into the sample tank,
183 which was pumped down to a vacuum below 10⁻⁴ Torr. Diffraction patterns were collected for
184 exposure times between 100 and 152 μAhours with ISIS operating at 40 Hz, an average proton
185 current of ~160 μA and upstream neutron choppers selecting one pulse in five.

186

187 Data were collected simultaneously in both the high-resolution backscattering and 90°
188 detector banks in the time-of-flight ranges 32000 μs to 126000 μs and 32000 μs to 130000 μs

189 respectively. Diffraction spectra were focused, binned as $\Delta t/t = 0.0005$ and 0.0003 for the $2\theta = 90^\circ$
190 and backscattering data respectively, background subtracted, normalised to the incident flux
191 distribution using the isotropic incoherent scattering from a V rod and finally corrected for
192 absorption and self-scattering. The resulting data were subsequently formatted for use in a two-
193 bank whole profile Rietveld refinement.

194

195 Structural refinement

196 Structural parameters were determined from whole pattern profile fitting of the diffraction
197 data within the GSAS (General Structure Analysis System) code of Larson and Von Dreele (1994)
198 interfaced with EXPGUI (Toby 2001). The first refinement for each sample was based upon the
199 structural model of Hofmeister et al. (2004) using coherent scattering lengths from Sears (1992) of
200 4.70 fm (Ca), 3.449 fm (Al), -3.438 fm (Ti), 5.38 fm (Mg) and 5.803 fm (O). Peak profiles were
201 modelled using the model-dependent Le Bail method with three sample-dependent variables and
202 backgrounds were modelled using a five-term shifted Chebyshev function. Thereafter, the structure
203 was refined using the Rietveld method (Rietveld 1969; 2000). The profiles from the two data banks
204 were scaled, the structural parameters of additional phases (if any) added and scaled relative to
205 hibonite, and then refined simultaneously. The unit-cell parameters for hibonite were refined first,
206 followed by the atomic coordinates and atomic displacement parameters (ADP).

207

208 Mg and Ti were initially included in the refinements based upon the stoichiometry calculated
209 by EDS and then varied as required by the refinement process. Ti site occupancies for the two Ti^{3+}
210 end-member samples (0.20,1.0) and (0.33,1.0) were allowed to vary within the least squares
211 refinements. For the Ti^{4+} end-member and the mixed-valent samples, however, the Mg and Ti site
212 occupancies were fixed during the least squares refinements and manually iterated between
213 refinement cycles. Attempts at discriminating between the fractional coordinates and ADPs of
214 different atoms on the same site were unsuccessful, and consequently the fractional coordinates and
215 ADPs for all atoms on a specific site were constrained to be identical. The proportions of Ti (or Mg)
216 and Al on a site were constrained to sum to 1, except for the M2 site where the cation is axially
217 displaced from the mirror plane and thus the maximum occupancy is 0.5.

218

219 Density functional theory modelling

220 DFT (Hohenberg and Kohn 1964; Kohn and Sham 1965) based calculations within the
221 generalised gradient approximation (GGA) were used to determine the energy and structure of a
222 range of Ti substitutions in hibonite. Along with pure $\text{CaAl}_{12}\text{O}_{19}$ hibonite, simulations of various
223 notionally isolated point defects were performed. Specifically, we considered the direct substitution

224 of Al by Ti^{3+} , the substitution of Al by Ti^{4+} coupled to a charge balancing substitution of Mg for Al,
225 and cases where small clusters of Ti defects form. The GGA functional of Perdew et al. (1996) was
226 used to describe exchange and correlation, and our calculations made use of the SIESTA
227 methodology and code (Soler et al. 2002), which takes advantage of a strictly localised atom-like
228 basis set and pseudopotentials to achieve good computational performance for large systems.

229

230 The basis sets and pseudopotentials for Ti, Mg, and O in the calculations were taken from
231 previous work on Ti incorporation in olivine (Berry et al. 2007; Walker et al. 2007), zircon (Tailby
232 et al. 2011), and the thermodynamics of qandilite (Palin et al. 2008), which encompass a wide range
233 of cation coordination environments. For Al we made use of the pseudopotential and basis set
234 derived for a study of the structure of γ -alumina (Paglia et al. 2005), while for Ca we used a basis
235 set optimised for the study of perovskite using the method of Junquera et al. (2001) with double
236 zeta polarised valance states (4s and 4p), single zeta polarised semi-core states (3s and 3p) and
237 added 3d states. The Ca pseudopotential was refitted from the version derived by Junquera et al.
238 (2001), which made use of the local density approximation, to GGA all-electron results using a
239 small partial core correction to avoid an undesirable kink in the fitted potential.

240

241 SIESTA makes use of a real space grid as an auxiliary basis for the calculation of the
242 exchange-correlation and Hartree energies. A kinetic energy cut-off of 250 Ry with $2 \times 2 \times 2$ grid
243 cell sampling was found to give sufficiently accurate results and minimise rippling artefacts. The
244 structure and energy of pure hibonite was derived from variable cell parameter calculations on a
245 single (64 atom) unit-cell. This calculation made use of a $5 \times 5 \times 2$ Monkhorst–Pack mesh in
246 reciprocal space. Calculations containing defects were all performed in a 256 atom supercell where
247 the lattice vectors were doubled in the x and y directions to give a minimum separation of 11.2 Å
248 between periodic images of any atom within the structural layers and a 22.0 Å separation along z .
249 These defect calculations only sampled reciprocal space at the Γ -point and the cell parameters were
250 not permitted to vary from those calculated for the perfect system (the defect calculations were thus
251 designed to simulate isolated point defects). Geometry optimisation was performed using the
252 Broyden and conjugate gradients algorithms with stop parameters of a maximum force of 0.01
253 eV/Å on any atom and (where the cell parameters were allowed to vary) a maximum stress of 200
254 bar on any component of the stress tensor.

255

256

Results

257 The eight samples studied by NPD encompass the full range of Ti^{3+} , Ti^{4+} , and ΣTi contents,
258 and $\text{Ti}^{3+}/\Sigma\text{Ti}$ that have been measured in meteoritic hibonite (Figure 2) as well as more Ti^{3+} -rich

259 and Ti⁴⁺-rich compositions.

260

261 Rietveld analysis

262 The results of the Rietveld refinement of the NPD data for all eight synthetic Ti-bearing
263 hibonite samples are given in Table 3 (lattice parameters and site occupancies) and Table 4 (atomic
264 coordinates, displacement parameters). The whole-profile Rietveld powder statistics (as defined by
265 Young, 1993) for the simultaneous refinement of the 90° and backscatter detector-bank datasets
266 were $wR_p = 2.3 - 3.4 \%$ and $R_p = 2.5 - 4.6 \%$. The observed, calculated and difference profiles for
267 the Ti³⁺ end-member sample (0.20,1.0) and the Ti⁴⁺ end-member sample (0.98,0) are shown in
268 Figure 3. Initially the Ti and Mg pfu were set to those determined by EDS but were allowed to vary
269 during the refinements. It seems reasonable to expect a 1:1 correlation between the Rietveld refined
270 and EDS determined Ti and Mg contents, and this was observed (Figure 4). In this work the refined
271 structural data are plotted against Mg and Ti pfu values from the Rietveld refinements.

272

273 Most of the Ti⁴⁺-bearing samples have a degree of compositional variability, as evident from
274 the large uncertainties of the Al₂O₃ and TiO₂ values (relative to those of the Ti³⁺ end-members) in
275 Table 2, which resulted in asymmetric peak broadening of their diffraction data. Two strategies
276 were applied to account for this peak asymmetry. Firstly, the variability in the Ti-content was
277 considered by incorporating a Ti-poor hibonite into the Rietveld model as a minor secondary phase.
278 Secondly, the refinements were performed assuming a homogeneous sample and accepting slightly
279 increased residuals and fit statistics. Both refinement strategies produced the same structural model
280 and Ti and Mg site-occupancies. The data presented in Tables 3 and 4, and discussed throughout
281 are those obtained using the second of these strategies.

282

283 Throughout the Rietveld analyses the ADPs were constrained to be isotropic. Single-crystal
284 XRD studies of CaAl₁₂O₁₉ have shown, however, that the ADP for the M2 cation is relatively
285 anisotropic with U₃₃ (parallel to z) four times larger than U₁₁ and U₂₂ (Hofmeister et al. 2004;
286 Utsunomiya et al. 1988). The degree of anisotropy determined for the M2 ADP in natural hibonite
287 that may contain additional cations, such as Ti, on the M2 site was found to be even larger
288 (Hofmeister et al. 2004; Nagashima et al. 2010). This anisotropy of the displacement parameter for
289 M2 relates to a combination of axial off-centring of the cation from the equatorial plane and
290 anisotropic thermal motion, although the static rather than dynamic contributions are likely to be
291 dominant (Nagashima et al. 2010). The ADP for the M2 cation in our refined models (U_{iso} in Table
292 4) is ~1.5 - 2 times larger than the average ADP for the cations on the four other M sites, consistent
293 with previous results (Bermanec et al. 1996; Hofmeister et al. 2004; Nagashima et al. 2010). In an

294 attempt to quantify the anisotropy of the M2 ADP, additional refinements were performed in which
295 the ADP for this site could vary anisotropically. While the results should be treated cautiously due
296 to the high degree of freedom in the refinement, it was found that the ADPs for M2 were distinctly
297 anisotropic with U_{33} being approximately double U_{11} and U_{22} .

298

299 DFT modelling

300 To provide a reference structure for the defect calculations, and as a test of the accuracy of the
301 methodology, SIESTA was first used to calculate the atomic positions and lattice parameters of
302 $\text{CaAl}_{12}\text{O}_{19}$ hibonite. The initial structure was based on the hibonite refinement reported by
303 Bermanec et al. (1996) with the impurities removed. The 5-coordinate M2 site deserves special
304 comment. In the $P63/mmc$ space group the three equatorial oxygen sites of this trigonal bipyramid
305 lie on a mirror plane but in hibonite the central M2 atom is displaced and, when averaged over a
306 large sample, the atomic occupancy is split evenly over two $4e$ sites. As a result, in any given
307 trigonal bipyramid the M2 Al atom is displaced ~ 0.3 Å in either the positive or negative z direction
308 and one of the $4e$ sites in the bipyramid is occupied and the other unoccupied. This locally breaks
309 the crystal symmetry (removing the mirror plane) and the partial occupancy reveals dynamic and
310 static averaging in the diffraction experiment. The SIESTA calculation describes an infinite array
311 of copies of a single unit-cell without this averaging. As there are two M2 sites in the unit-cell
312 there are two possible structures: one with the M2 Al atoms displaced in the same z direction (~ 11.1
313 Å M2-M2 spacing along c) and one where they are displaced in opposite directions (alternating
314 ~ 10.9 and ~ 11.4 Å spacing along z). Both starting structures were investigated and it was found
315 that while the distortion was preserved in the DFT calculations (i.e. the Al atom did not move to the
316 mirror plane) the structures had equal energies. This is consistent with the presence of disorder on
317 this site as indicated by the ADPs and partial site occupancies. Having generated the starting
318 hibonite structures, energy minimisation was undertaken in which the lattice parameters and atomic
319 positions were allowed to vary with no symmetry imposed. This process yielded lattice parameters
320 of $a = b = 5.61$ Å, $c = 22.05$ Å, $\alpha = \beta = 90.0^\circ$, and $\gamma = 120.0^\circ$. The larger lattice parameters (by
321 $\sim 1\%$) compared to the experimental determination of Hofmeister et al. (2004) are expected for DFT
322 calculations utilising a GGA functional.

323

324 The structure of the optimised cell was used to build the 256 atom supercell for defect
325 calculations. Six sets of defect calculations were performed. (1) An Al atom on each of the five M
326 sites was replaced in turn by a Ti atom leading to the isovalent substitution of Al^{3+} by Ti^{3+} . (2)
327 Each of these calculations was repeated with one less electron in the simulation cell giving a
328 positively charged system and describing the substitution of Al^{3+} by Ti^{4+} . (3) Each of the isovalent

329 calculations was also repeated with the Ti atom being replaced by a Mg^{2+} giving a negatively
330 charged system with Mg^{2+} substituting for Al^{3+} . (4) One Al atom was replaced by Ti and one by
331 Mg leading to the charge-neutral coupled substitution of two Al^{3+} for a Ti^{4+} and Mg^{2+} . For each M
332 site occupied by Al there are several inequivalent ways of introducing the Mg to make a coupled
333 substitution. Every case where the Ti and Mg polyhedra share a face, edge or vertex (21 distinct
334 coupled defects) was investigated and, guided by the results of the calculations on isolated Ti^{4+} and
335 Mg^{2+} substitutions, three cases where the Mg is on a M3 site with the Ti on a nearby M2 or M4 site
336 (M3 does not share a vertex with M2 or M4) were also considered. (5) Two Ti atoms were placed
337 on adjacent Al sites to give neutral two-atom defect clusters (nominally of Ti^{3+} ions). (6) Two Ti
338 and two Mg atoms were added to form neutral four-atom clusters (nominally containing Ti^{4+} ions).
339 In cases (5) and (6), only a small subset of the vast number of possible atomic configurations were
340 considered with the choice based on the earlier calculations, the generation of simple structures and
341 the NPD results. Each defect configuration was subjected to geometry optimisation that allowed all
342 atomic positions (but not the lattice parameters) to vary in order to evaluate the defect stability.
343 Energies are given in Tables 5 and 6 where the defect structures are described using Kröger-Vink
344 notation.

345

346 *Isolated defects*

347

348 If Ti substitutes as isolated trivalent ions it will dominantly occupy the 5-coordinate M2 site
349 as this incorporation mechanism has the lowest energy (Table 5). The energies of the charged cells
350 containing isolated Mg^{2+} and Ti^{4+} ions suggest that, if the necessary charge balancing defect can be
351 assumed to not alter the structure or energy of the defect site, Mg^{2+} will occupy the M3 site and Ti^{4+}
352 will occupy the M2 site.

353

354 As well as energies, the SIESTA calculations also yield the detailed structure of each defect.
355 Considering isolated defects, the Ti atom in the $\text{Ti}_{\text{Al}2}^{\text{x}}$ defect is located close to the ideal mirror
356 plane and, unlike Al on the M2 site, is not significantly displaced along z . There are thus two Ti-O1
357 bonds of approximately the same length (2.231 and 2.237 Å), which are between the short (2.062
358 Å) and long (2.357 Å) bond lengths calculated for Al on this site. However, the threefold rotation
359 axis normal to the equatorial plane of the M2 trigonal bipyramid is broken when Ti^{3+} is present on
360 the site. Instead of three 1.769 Å Al-O3 bonds the three Ti-O3 bonds are 1.903, 1.916 and 1.841 Å.
361 The average Ti-O bond length is thus slightly longer than the average Al-O bond length, both
362 calculated using DFT (2.03 Å versus 1.95 Å). In contrast, the Ti^{4+} defect on the M2 site does not
363 break this 3-fold rotational symmetry. Ti^{4+} is also located close to the mirror plane with the two Ti-

364 O1 bonds having lengths of 2.169 and 2.175 Å. The three Ti-O3 bonds are 1.806 Å, resulting in an
365 average Ti⁴⁺-O bond length of 1.95 Å, which is equal to the Al-O bond length for this site.

366

367 *Ti-Mg interactions*

368 Coulombic interactions will penalise the formation of the isolated Ti⁴⁺ and Mg²⁺ defects
369 considered above and while these may tend to be entropically stabilised, especially at high
370 temperatures and low impurity concentrations, the formation of charge-neutral defect clusters is
371 perhaps more realistic for the samples synthesized in this study. In order to consider this
372 possibility, charge-neutral simulation super-cells were constructed containing both Ti and Mg on M
373 sites that are close together. The energies of these simulation cells after geometry optimisation are
374 reported in Table 6. These data show that the most stable configuration for a Ti⁴⁺ defect charge-
375 balanced by a Mg²⁺ defect is for Mg²⁺ to occupy an M3 site and Ti⁴⁺ to occupy either an M2 or M4
376 site, with the M2 site being the lower energy configuration. Importantly, the energy does not
377 correlate with the Ti⁴⁺ - Mg²⁺ separation; indeed the Ti⁴⁺ and Mg²⁺ polyhedra do not share vertices
378 in the lowest energy configurations. These configurations have Ti⁴⁺ and Mg²⁺ on the M sites that
379 are the lowest energy incorporation mechanisms for the isolated impurities. This indicates that the
380 locations of Ti⁴⁺ and Mg²⁺ in the charge-neutral defect cluster are controlled by the elemental site
381 preference, and not by short-range interactions between the defects. The energies reported in Tables
382 5 and 6 can be used to determine if these cluster defects are favorable relative to the isolated defects
383 by evaluating the binding energy, which is the energy change of the reaction:



385 or, using Kröger-Vink notation to specify the defect sites:



387 When evaluating the energy of this reaction it is important to account for the Coulombic interaction
388 between charged defects in the periodic replicas of the supercells on the right-hand side. This
389 contribution to the energy only varies slowly with supercell size and the important leading term can
390 be removed using the approach described for cubic systems by Leslie and Gillan (1985) and, for the
391 general case, by Woodley et al. (2003). The approach is to approximate the interaction as the energy
392 of an infinite periodic array of point charges, with the same geometry and charge as the point
393 defects, embedded in a dielectric continuum and to subtract this energy from the energy of the
394 defect-bearing supercells. Unfortunately, we do not know the static relative permittivity of hibonite
395 but we can place bounds on the magnitude of the binding energy between the Ti⁴⁺ and Mg²⁺ point
396 defects. An upper bound of 1.92 eV (~124 kJ/mol Ti) is obtained by neglecting the correction term
397 and a lower bound of 0.49 eV (~47 kJ/mol Ti) results from the minimum shielding that is likely to
398 be provided by the hibonite crystal (i.e. assuming a reasonable lower bound on the relative
399 permittivity of 3.0 and applying this to the full correction from the energy of a periodic array of ions

400 with unit charge in a vacuum, which is -1.1797 eV per charged supercell). Even for the lower bound
401 the formation of $\{\text{Ti}_{\text{Al}(2)}^{\bullet}\text{Mg}_{\text{Al}(3)}^{\prime}\}_{(b)}$ is of lower energy than the isolated $\text{Ti}_{\text{Al}(2)}^{\bullet}$ and $\text{Mg}_{\text{Al}(3)}^{\prime}$ defects
402 and thus bound defects are expected to dominate.

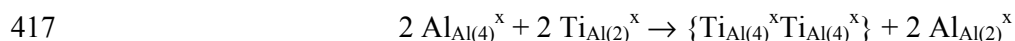
403

404 *Ti-Ti interactions*

405 The concentration of Ti in the samples with high Ti contents is such that the defects must, on
406 purely geometrical grounds, be close together and thus interact. Calculations were performed to
407 investigate, for both Ti^{3+} and Ti^{4+} , if Ti-Ti interactions alter the structure or energetics of the defects
408 and if the interactions provide a driving force for Ti clustering. Based on the energies of the
409 isolated Ti^{3+} defects and the results of the NPD study, a likely configuration for stabilising pairs of
410 bound Ti^{3+} impurities is for these ions to occupy adjacent M4 sites, as these are low-energy isolated
411 defect sites that share faces in the structure. The energy and structure of this $\{\text{Ti}_{\text{Al}(4)}^{\times}\text{Ti}_{\text{Al}(4)}^{\times}\}$ defect
412 was calculated and the nature of the Ti – Ti interaction found by considering the energy of the
413 reaction:



415 where the left hand side represents the lowest energy isolated Ti^{3+} impurities and the right hand side
416 the coupled defect structure. In Kröger-Vink notation this reaction can be written as:



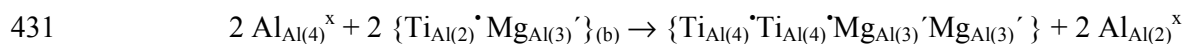
418 Using the data in Tables 5 and 6, the energy change of this reaction is -1.72 eV (83 kJ/mol of Ti)
419 and Ti^{3+} impurities are thus expected to occupy adjacent face-sharing M4 octahedra.

420

421 Similar calculations were performed to investigate the possibility of clustering of Ti^{4+}
422 impurities. An added complication in this case is the need for charge balancing Mg^{2+} defects, which
423 on the basis of the energies of the various isolated defects and the NPD results are found on the M3
424 site. The simplest starting configuration for such a two- Ti^{4+} , two- Mg^{2+} defect cluster is to place one
425 Mg^{2+} in the spinel layer above two Ti^{4+} defects on M4 sites and one Mg^{2+} in the spinel layer below
426 the Ti^{4+} defects. The four defects in the cluster thus form a line parallel to z and have no net dipole.
427 The stability of this $\{\text{Ti}_{\text{Al}(4)}^{\bullet}\text{Ti}_{\text{Al}(4)}^{\bullet}\text{Mg}_{\text{Al}(3)}^{\prime}\text{Mg}_{\text{Al}(3)}^{\prime}\}$ configuration is found by considering the
428 energy of the reaction:



430 or, in Kröger-Vink notation:



432 which is -0.32 eV (15 kJ/mol of Ti). This low binding energy suggests that Ti^{4+} defect clustering
433 will be limited to high Ti contents and low temperatures. This is consistent with the NPD results

434 for samples with high Ti contents, which show that Ti^{4+} preferentially occupies the M4 site, and
435 indicates that Ti site occupancies might change with Ti concentration.

436 The computational results are all for defects at zero Kelvin in the dilute limit. The potential
437 effects of higher temperatures and defect concentrations arise from configurational entropy, which
438 may allow non-ground state defect sites to become occupied. For the single isolated defects this
439 effect can be relatively easily explored using elementary Boltzmann statistics, knowledge of the
440 energy difference between the defect sites, and the site multiplicities. For Mg^{2+} the large (0.83 eV;
441 ~80 kJ/mol of Mg) energy difference between substitution at M3 and the other sites means that
442 essentially all Mg^{2+} is expected to be found on this site at all realistic temperatures. For the single
443 isolated Ti^{3+} and Ti^{4+} defects, where the difference in energy between different sites is lower, we
444 only find significant occupancies (>20%) of sites other than M2 above 1500 K. For the defect
445 clusters only a small subset of the enormous number of possible Ti^{3+} , Ti^{4+} and Mg defect cluster
446 configurations have been considered and this makes quantification of the site occupancies as a
447 function of temperature and Ti content impossible. One approach, which is beyond the scope of the
448 current study, would be to use DFT calculations to parameterize an effective Hamiltonian for cation
449 interactions that is subsequently used as input to Monte Carlo simulations of defect clustering and
450 site occupancy as a function of temperature (e.g. Warren et al. 2001, Palin et al. 2008). However,
451 even without such a study we can make qualitative predictions of the likely effects. Increasing
452 temperature will always make the entropic contribution more important and tend to break up defect
453 clusters and allow multiple different defect configurations to co-exist. Increasing the Ti content will
454 have the opposite effect and tend to result in more clustering of defects; but these effects cannot be
455 quantified without explicit calculations involving all possible defect configurations. One problem
456 that would significantly complicate such a study is the possibility of interactions between Ti^{3+} and
457 Ti^{4+} defects, as the self-interaction problem in DFT will lead to excessive electron delocalization
458 and equalization of the charge on the two defects (e.g. Cramer and Truhlar 2009).

459

460

Discussion

461 Site occupancy analysis

462 The site occupancies determined from the refinements of the NPD data are unambiguous and
463 define the substitution mechanisms of Ti^{3+} and Ti^{4+} into these hibonite samples (Table 3). There
464 were no prior assumptions regarding which sites Ti^{3+} , Ti^{4+} and Mg^{2+} would occupy and refinements
465 were attempted with these cations occupying each M site in turn. All models in which Ti and Mg
466 were placed on any site other than those in Table 3 resulted in rapidly diverging refinements or
467 strongly non-physical structural parameters. For the Ti^{3+} end-member samples, (0.20,1.0) and
468 (0.33,1.0), Ti only occupies the face-sharing M4 octahedral site. For the Ti^{4+} end-member samples,

469 (0.44,0) and (0.98,0), Ti occupies both the M4 and trigonal bipyramidal M2 sites, while Mg^{2+} only
470 occupies the tetrahedral M3 site. In the mixed-valent samples Ti occupies the M2 and M4 sites and
471 Mg^{2+} is again exclusively located on M3. The refinements do not explicitly distinguish Ti^{3+} from
472 Ti^{4+} , however, there is no reason to expect that the substitution mechanisms identified for Ti^{3+} and
473 Ti^{4+} cannot be applied to the mixed-valent samples. Accordingly, within the mixed-valent hibonites
474 we suggest that Ti^{3+} only occupies M4 and Ti^{4+} occupies both the M2 and M4 sites.

475

476 For the samples in this study it is reasonable to expect that Ti^{4+} undergoes a coupled
477 substitution with Mg^{2+} to maintain charge balance within the structure and that Ti^{4+} pfu = Mg^{2+} pfu.
478 Given that Ti^{3+} only occupies M4 while all the Ti on M2 is Ti^{4+} , the proportions of Ti^{3+} and Ti^{4+} on
479 M4 can then be calculated (Table 3). The Ti^{4+} occupancies of M2 and M4 increase linearly as a
480 function of Ti^{4+} content irrespective of whether the samples are Ti^{4+} end-members or mixed-valent
481 (Figure 5a,b). Furthermore, the partitioning of Ti^{4+} between the M2 and M4 sites appears to be
482 consistent across the entire suite of samples (Table 3), with an average of 0.18 ± 0.02 , irrespective
483 of the concentration of Ti and the Ti^{3+}/Ti^{4+} ratio. The DFT site predictions for Ti^{4+} also indicate a
484 preference for M4 over M2, although the predicted preference is not as strong as that observed by
485 NPD. This difference may be attributed to the different Ti contents in each case, suggesting that
486 Ti^{4+} site occupancy could be influenced by concentration. In studies of terrestrial hibonite using
487 single crystal XRD Ti^{4+} has been reported to occupy both the M2 and M4 sites (Nagashima et al.
488 2010) but also only the M4 site (Bermanec et al. 1996). The ratio of the partitioning of Ti^{4+}
489 between M2 and M4 reported by Nagashima et al. (2010) is 0.39, which is double the average value
490 of that found here. These discrepancies can be attributed to the refined occupancies of Ti^{4+} on M2.
491 The refined structure of Nagashima et al. (2010) has 0.62 Ti pfu, compared to the chemical formula
492 of the hibonite crystal which has with 0.52 Ti pfu. Additionally, the crystal contained up to 0.04
493 pfu of Fe, which was not included in the refinement. As Fe is a stronger scatterer of X-rays than Ti,
494 the modelling of a significant amount of Fe by Ti on a single site is likely to cause an artificially
495 increased Ti occupancy in order to compensate for the reduced scattering from that site in the
496 structural model. The crystal of Bermanec et al. (1996) contained 0.3 Fe pfu, which was found to
497 occupy the M2 site. Given that the proportion of Fe on M2 is an order of magnitude greater than
498 that expected for Ti, the Fe would mask the presence of Ti. It is also possible that the large
499 proportion of Fe on M2 precluded the substitution of Ti onto this site (Kreber and Gonser 1976).

500

501 The refinements of the NPD data clearly show that all Mg^{2+} occupies the tetrahedral M3 site.
502 This is supported by DFT calculations (Table 5), which indicate that this is the most stable site for
503 Mg^{2+} by 0.83 eV (~ 80 kJ/mol of Mg). In previous studies of hibonite and structurally similar

504 compounds (Table 1; Abrahams et al. 1987) Mg could only be inferred to occupy the tetrahedral
505 site due to the difficulty of distinguishing between Mg and Al by XRD.

506

507 Optical absorption spectra of both natural and synthetic Ti- and Mg-bearing blue hibonite
508 exhibit a strong absorption band at 715 nm, the intensity of which has been used to infer f_{O_2}
509 (Ihinger and Stolper 1986). It was argued that Ti^{3+} did not occupy an octahedral site because this
510 absorption band differed in energy from that of Ti^{3+} in octahedral coordination in Al_2O_3 . Instead
511 Ti^{3+} was thought to occupy the five-coordinate M2 site (Burns and Burns 1984). The absorption
512 spectra of Ti^{3+} - and Ti^{4+} -bearing Al_2O_3 , however, exhibit a strong band near 750 nm assigned to
513 Ti^{3+} - Ti^{4+} interactions (Sanchez et al. 1988; Aggarwal et al. 1988; Yamaga et al. 1994). Similar
514 interactions could produce the 715 nm absorption band in hibonite given that both Ti^{3+} and Ti^{4+}
515 occupy the M4 site and that neighbouring M4 octahedra form isolated face-sharing pairs.

516

517 The orientation dependence of ESR spectra recorded for a single crystal of meteoritic hibonite
518 found that the maximum g -tensor was parallel to the c -axis (Beckett et al. 1988). These spectra are
519 similar to those of Ti^{3+} -doped β -alumina, in which Ti^{3+} occurs in rhombically distorted octahedral
520 coordination and the orientation of the g -tensor maximum does not correspond to the direction of
521 maximum site distortion as expected, but is collinear with the Al-Al direction (Barret et al. 1985).
522 That is, the orientation of the g -tensor maximum is consistent with the presence of a next nearest
523 neighbour Ti, as expected for Ti occurring as clustered pairs (Yamaga et al. 1994). M4 in hibonite
524 is a rhombically distorted octahedral site and forms face sharing pairs such that the short M4-M4
525 cation direction is parallel to the crystallographic c -axis. As a result, the ESR data of Beckett et al.
526 (1988) can be re-interpreted as indicating that Ti^{3+} occupies the M4 site with the g -tensor maximum
527 corresponding to the Ti-Ti interaction parallel to the c -axis, and thus is in agreement with the NPD
528 model.

529

530 NPD shows that Ti^{3+} occupies the M4 site in hibonite, and furthermore, our DFT calculations
531 and optical absorption and ESR spectra in the literature are consistent with Ti^{3+} occupying M4 such
532 that Ti-Ti interactions occur across the shared face of the $M4_2O_9$ pairs. Indeed, the DFT
533 calculations show a stabilization energy of ~ 83 kJ/mol for such Ti^{3+} - Ti^{3+} interactions. DFT also
534 suggests that a clustering model involving Ti^{4+} on M4 sites is favourable relative to isolated Ti^{4+}
535 defects. What is not clear, however, is whether Ti^{3+} - Ti^{3+} and/or Ti^{4+} - Ti^{4+} interactions are favoured
536 over Ti^{3+} - Ti^{4+} interactions, an issue that is beyond the scope of the DFT calculations performed and
537 difficult to resolve with NPD. Nevertheless it is an important issue, for while the characteristic blue
538 colour of many meteoritic hibonites is related to the presence of Ti^{3+} , the intensity of this colour

539 will not be a good indicator of the concentration of Ti^{3+} , or the $\text{Ti}^{3+}/\text{Ti}^{4+}$ ratio, if Ti^{3+} is involved in
540 more than one type of Ti-Ti interaction. Moreover, the strong feature at 715 nm present in optical
541 absorption spectra is not simply related to the amount of Ti^{3+} , but to the number of $\text{Ti}^{3+}-\text{Ti}^{4+}$
542 interactions, which may not equate to the amount of Ti^{3+} .

543

544 Structural modifications

545 The larger sizes of Ti^{3+} and Ti^{4+} relative to Al^{3+} (Shannon 1976) suggest that the
546 incorporation of Ti will cause an expansion of the unit cell. Indeed, the increase in the refined unit
547 cell parameters as a function of Ti is essentially linear (Table 3, Figure 6a,b). The increase in the
548 size of the unit cell as a function of Ti pfu is not isotropic and the c/a ratio decreases linearly with
549 increasing Ti (Figure 6c). Also shown in Figure 6 are the unit cell parameters of synthetic
550 $\text{CaAl}_{12}\text{O}_{19}$ (Hofmeister et al. 2004), synthetic Ti^{3+} -bearing $\text{CaAl}_{10.1}\text{Ti}_{1.9}\text{O}_{19}$ (Wittmann et al. 1958)
551 and terrestrial Ti^{4+} hibonite (Nagashima et al. 2010). The a and c parameters of $\text{CaAl}_{10.1}\text{Ti}_{1.9}\text{O}_{19}$
552 (Wittmann et al. 1958) are clearly displaced from the trends defined by the other samples (Figure
553 6a, b). If the cell parameters and chemistry of this sample are accurate, then the rate of increase of
554 the unit-cell parameters as a function of Ti pfu is smaller for Ti^{3+} end-member hibonites than for
555 Ti^{4+} -bearing hibonites. Certainly the increase in the unit-cell parameters relative to $\text{CaAl}_{12}\text{O}_{19}$ of
556 the two Ti^{3+} end-member hibonites of this study is very small. The difference in unit-cell
557 parameters as a function of Ti pfu for the Ti^{3+} end-member and Ti^{4+} -bearing hibonites is not related
558 to the relative sizes of the two Ti cations but is more likely to be associated with the additional
559 complexity of the Ti^{4+} substitution mechanism, which involves both Mg^{2+} and Ti^{4+} and the M2, M3
560 and M4 sites. The unit-cell parameters of the mixed-valent samples are collinear with those of the
561 Ti^{4+} samples both as a function of total Ti pfu (Figure 6) and also as a function of Ti^{4+} pfu (Figure
562 7). This strongly suggests that the driving force for the greater rate of increase of the unit-cell
563 parameters for the Ti^{4+} end-members relative to the Ti^{3+} end-members predominates in the mixed-
564 valent samples.

565

566 With Ti being accommodated only in the R-block layers it may be expected that distortions in
567 this layer will dominate the expansion of the unit cell as a function of increasing Ti ($c > a$). This,
568 however, is not the case with the expansion parallel to z being dominated by the S-block. Indeed,
569 the expansion of the R-block along z (given by the O1-O1 distance) appears to be negligible across
570 most of the series (Table 7), with a measurable expansion only occurring in the sample with the
571 largest Ti pfu, (1.37, 0.39), where $>50\%$ of the M4-M4 pairs are Ti-Ti rather than Al-Al. The c
572 unit-cell edge comprises two R-blocks and two S-blocks and although the S-block is only directly
573 involved in the substitution of Ti into hibonite through occupancy of M3 by Mg^{2+} , this structural

574 unit accounts for the entire expansion of the c parameter (Figure 6, Table 7) for all samples except
575 (1.37, 0.39). As Mg^{2+} is larger than Al^{3+} (Shannon 1976) the interatomic distances within M3
576 increase linearly as a function of Mg^{2+} , and are inherently a good indicator of the amount of Ti^{4+} in
577 a hibonite structure (Figure 8). The M3-O2 distance, which is parallel to z , expands by twice as
578 much as the M3-O4 distance, and the $\sim 0.1 \text{ \AA}$ by which M3-O2 expands across the series accounts
579 for the total expansion of the c unit cell edge ($\sim 0.2 \text{ \AA}$), which contains two M3-O2 distances. This
580 suggests that other structural modifications within this unit do not contribute to changes in the unit
581 cell. The M5O_6 octahedra connect the M3 sites, into which Mg^{2+} substitutes, and the R-block, into
582 which Ti substitutes. As such M5O_6 is sensitive to the effects of both Mg^{2+} and Ti^{4+} substituting
583 into hibonite and the M5-O distances vary linearly towards $\sim 1.9 \text{ \AA}$ as a function of Ti^{4+} (Figure 9).
584

585 Within the R-block the M2-O1a and M2-O1b distances decrease and increase linearly as a
586 function of Ti pfu respectively (Figure 10a,b). Consequently, the axial off-centring of the M2 cation
587 also increases linearly as a function of Ti. Furthermore, there is a concomitant increase in the
588 equatorial M2-O3 distances (Table 7). As only Ti^{4+} is replacing Al^{3+} on the M2 site, it may be
589 possible to resolve the influence of Ti^{4+} directly upon the observed structural modifications within
590 the M2O_5 polyhedra. While the M2-O distances and the axial off-centring of the M2 cation all vary
591 linearly with Ti^{4+} (e.g. Figure 10c) there is no correlation with Ti^{3+} . With both Ti^{3+} and Ti^{4+}
592 substituting onto the M4 sites and Ti-Ti interactions occurring across the shared face of the $\text{M4}_2\text{O}_9$
593 pairs it is not possible to resolve individual Ti^{3+} - or Ti^{4+} -dependent variations in the interatomic
594 distances within the M4O_6 octahedra. However, the M4-M4 distance across the shared face of the
595 $\text{M4}_2\text{O}_9$ pairs increases linearly as a function of Ti^{4+} pfu (Figure 11a). Constrained by the non-
596 varying thickness of the R-block as a function of Ti, the linear expansion of the M4-O3 distance
597 with Ti is offset by the linear decrease in the M4-O5 distance as a function of Ti^{4+} (Figure 11b,c),
598 aside from sample (1.37, 0.39) where $>50\%$ of the M4 sites are Ti rather than Al.

599

600

Implications

601 Hibonite has been proposed as a single mineral oxybarometer that can provide an indication
602 of the f_{O_2} conditions prevalent at the time of its formation either within the early solar nebula or
603 during some later reprocessing event (Ihinger and Stolper 1986; Beckett et al. 1988). Hibonite
604 oxybarometry has been attempted for CAIs within the Murchison and Allende carbonaceous
605 chondrites. Estimates of f_{O_2} determined by optical absorption spectroscopy are up to 10 times more
606 oxidised than those expected in the solar nebula (Ihinger and Stolper 1986), while those from ESR
607 spectroscopy span nine orders of magnitude (Beckett et al. 1988). Both of these approaches are
608 strongly dependent upon a crystal chemical model in which Ti^{3+} occupies the five-coordinate M2

609 site. However, the Rietveld and DFT results of the present study show conclusively that Ti^{3+}
610 occupies the octahedral face-sharing M4 site. Furthermore, DFT calculations find that Ti^{3+} - Ti^{3+}
611 interactions between M4 octahedral pairs are favoured with respect to Al^{3+} - Ti^{3+} interactions, while
612 the substitution mechanisms identified by NPD suggest that Ti^{4+} - Ti^{4+} and Ti^{4+} - Ti^{3+} interactions may
613 also occur. Reinterpretation of the optical and ESR spectra in light of these results indicate that the
614 spectral features utilised for hibonite oxybarometry are not associated with occupancy of M2 by
615 Ti^{3+} , but actually arise from Ti-Ti interactions. When interpreting spectroscopic data in terms of
616 $\text{Ti}^{3+}/\Sigma\text{Ti}$ and f_{O_2} the existence of Ti-Ti interactions, which may not be simply related to the amount
617 of Ti^{3+} , need to be considered.

618

619 In this study, hibonite samples with $\text{Ti}^{3+}/\Sigma\text{Ti}$ ranging from 0.27 to 1.0 were all prepared at the
620 same f_{O_2} ($\log f_{\text{O}_2} = -16$ at 1400 °C or 6.3 log units below the iron-wüstite f_{O_2} buffer). This
621 illustrates how Ti^{4+} can be stabilised in hibonite by Mg^{2+} even under very reducing conditions. That
622 is, crystal chemistry can stabilise oxidation states independently of f_{O_2} . The $\text{Ti}^{3+}/\Sigma\text{Ti}$ ratio of
623 meteoritic hibonite is thus not necessarily related to the f_{O_2} of formation and will be strongly
624 influenced by composition. Furthermore, the placement of an upper limit on f_{O_2} based solely upon
625 the blue colour of a crystal of hibonite (Ihinger and Stolper 1986) may need to be reconsidered if
626 crystal chemical controls are able to stabilize Ti^{3+} under nominally oxidising conditions.

627

628

629

Acknowledgements

630

631

632

633

634

635

636

637

638

639

640

AJB thanks the Engineering and Physical Sciences Research Council (EPSRC) for the award of a CNE studentship, which was used to support PMD. The NPD experiments were facilitated by a beamtime award from ISIS Neutron Spallation Source (RB920090). The authors are grateful for the help of J. Najorka, J. Spratt, A.T. Kearsley and the support of many ISIS staff. The computational part of this work made use of the facilities of HECToR, the UK's national high-performance computing service, which is provided by UoE HPCx Ltd at the University of Edinburgh, Cray Inc and NAG Ltd, and funded by the Office of Science and Technology through EPSRC's High End Computing Programme.

References

- 641
642 Abrahams, S.C., Marsh, P. and Brandle, C.D. (1987) Laser and phosphor host $\text{La}_{1-x}\text{MgAl}_{11+x}\text{O}_{19}$ (x
643 = 0.050): Crystal structure at 295 K. *Journal of Chemical Physics*, 86, 4221-4227.
644
- 645 Aggarwal, R.L., Sanchez, A., Stuppi, M.M., Fahey, R.E., Strauss, A.J., Rapoport, W.R. and
646 Khattak, C.P. (1988) Residual infrared-absorption in as-grown and annealed crystals of $\text{Ti-Al}_2\text{O}_3$.
647 *IEEE Journal of Quantum Electronics*, 24, 1003-1008.
648
- 649 Allen, J.M., Grossman, L., Davis, A.M. and Hutcheon, I.D. (1978) Mineralogy, textures and mode
650 of formation of a hibonite-bearing Allende inclusion. *Proceedings of the 9th Lunar and Planetary*
651 *Science Conference*, 1, 1209-1233.
652
- 653 Amelin, Y., Krot, A.N., Ulyanov, A.A. and Hutcheon, I.D. (2002) Lead isotopic ages of chondrules
654 and calcium-aluminium-rich inclusions. *Science*, 297, 1678-1683.
655
- 656 Armstrong, J.T., Meeker, G.P., Huneke, J.C. and Wasserburg, G.J. (1982) The Blue Angel: I. The
657 mineralogy and petrogenesis of a hibonite inclusion from the Murchison meteorite. *Geochimica et*
658 *Cosmochimica Acta*, 46, 575-595.
659
- 660 Barret, J.P., Gourier, D. and Vivien, D. (1985) Influence of titanium impurities on the chemical
661 alteration of β - and β'' -alumina in sodium environment. *ESR study. Solid State Ionics*, 15, 127-134.
662
- 663 Beckett, J.R., Live, D., Tsay, F.-D., Grossman, L. and Stolper, E. (1988) Ti^{3+} in meteoritic and
664 synthetic hibonite. *Geochimica et Cosmochimica Acta*, 52, 1479-1495.
665
- 666 Bermanec, V.V., Holtstam, D., Sturman, D., Criddle, A.J., Back, M.E. and Scavnicar, S. (1996)
667 Nezilovite, a new member of the magnetoplumbite group, and the crystal chemistry of
668 magnetoplumbite and hibonite. *The Canadian Mineralogist*, 34, 1287-1297.
669
- 670 Berry, A.J., Danyushevsky, L.V., O'Neill, H.St.C., Newville, M. and Sutton, S.R. (2008) Oxidation
671 state of iron in komatiitic melt inclusions indicates hot Archaean mantle. *Nature*, 455, 960-963.
672
- 673 Berry, A.J., Walker, A.M., Hermann, J., O'Neill, H.St.C., Foran, G.J. and Gale, J.D. (2007)
674 Titanium substitution in forsterite. *Chemical Geology*, 242, 176-186.
675 doi:10.1016/j.chemgeo.2007.03.010.

676

677 Bettman, M. and Peters, C.R. (1969) The crystal structure of $\text{Na}_2\text{O} \cdot \text{MgO} \cdot 5\text{Al}_2\text{O}_3$ with reference to
678 $\text{Na}_2\text{O} \cdot 5\text{Al}_2\text{O}_3$ and other isotypal compounds. *Journal of Physical Chemistry*, 73, 1774-1780

679

680 Bischoff, A. and Srinivasan, G. (2003) ^{26}Mg excess in hibonites of the Rumuruti chondrite Hughes
681 030. *Meteoritics and Planetary Science*, 38, 5-12.

682

683 Burns, R.G. and Burns, V.M. (1984) Crystal chemistry of meteoritic hibonites. *Journal of*
684 *Geophysical Research*, 89, 313-321.

685

686 Cramer, C. J. and Truhlar, D. G. (2009) Density functional theory for transition metals and
687 transition metal chemistry. *Physical Chemistry Chemical Physics*, 11, 10757-10816.

688

689 Curien, H., Guillemin, C., Orcel, J. and Sternberg, M. (1956) La hibonite, nouvelle espèce minérale.
690 *Comptes Rendus de l'Académie des Sciences, Paris*. 2845-2847.

691

692 Davis, A.M., Tanaka, T., Grossman, L., Lee, T. and Wasserburg, G.J. (1982) Chemical composition
693 of HAL, an isotopically-unusual Allende inclusion. *Geochimica et Cosmochimica Acta*, 46, 1627-
694 1651.

695

696 De Aza, A.H., Iglesias, J.E., Pena, P. and De Aza, S. (2000) Ternary system Al_2O_3 - MgO - CaO : Part
697 II, phase relationships in the subsystem Al_2O_3 - MgAl_2O_4 - CaAl_4O_7 . *Journal of the American Ceramic*
698 *Society*, 83, 919-927.

699

700 Doyle, P.M. (2012) Ti substitution mechanisms in hibonite and the determination of $\text{Ti}^{3+}/\text{Ti}^{4+}$ by X-
701 ray absorption spectroscopy for use as an oxybarometer with application to early Solar System
702 processes. PhD Thesis, Imperial College London.

703

704 Du, L.L. and Stebbins, J.F. (2004) Calcium and strontium hexaluminates: NMR evidence that
705 "pentacoordinate" cation sites are four-coordinated. *The Journal of Physical Chemistry. B,*
706 *Condensed Matter, Materials, Surfaces, Interfaces & Biophysical*, 108, 3681-3685.

707

708 Fuchs, L.H., Olsen, E. and Jensen, K.J. (1973) Mineralogy, mineral-chemistry, and composition of
709 the Murchison (C2) meteorite. *Smithsonian Contributions to the Earth Sciences*, 10, 1-39.

710

- 711 Graetsch, H.H. and Gebert, W. (1995) Cation distribution in magnetoplumbite type $\text{SrTi}_6\text{Co}_6\text{O}_{19}$.
712 *Zeitschrift für Kristallographie, Kristallgeometrie, Kristallphysik, Kristallchemie*, 210, 9-13.
713
- 714 Graetsch, H.H. and Gebert, W. (1996) Short Cr^{3+} - Cr^{3+} distances in magnetoplumbite type
715 $\text{SrCr}_9\text{Ga}_3\text{O}_{19}$. *Zeitschrift für Kristallographie, Kristallgeometrie, Kristallphysik, Kristallchemie*,
716 211, 25-30.
717
- 718 Grey, I.E., Madsen, I.C. and Haggerty, S.E. (1987) Structure of a new upper-mantle,
719 magnetoplumbite-type phase, $\text{Ba}[\text{Ti}_3\text{Cr}_4\text{Fe}_4\text{Mg}]\text{O}_{19}$. *American Mineralogist*, 72, 633-636.
720
- 721 Grossman, L., Beckett, J.R., Fedkin, A.V., Simon, S.B. and Ciesla, F.J. (2008) Redox conditions in
722 the solar nebula: observational, experimental, and theoretical constraints. *Mineralogical Society of*
723 *America: Reviews in Mineralogy and Geochemistry* 68, 93-140.
724
- 725 Hohenberg, P. and Kohn, W. (1964) Inhomogeneous electron gas. *Physical Review*, 136, 864-871.
726
- 727 Hofmeister, A.M., Wopenka, B. and Locock, A.J. (2004) Spectroscopy and structure of hibonite,
728 grossite, and CaAl_2O_4 : Implications for astronomical environments. *Geochimica et Cosmochimica*
729 *Acta* 68, 4485-4503.
730
- 731 Holtstam, D. (1996) Iron in hibonite: a spectroscopic study. *Physics and Chemistry of Minerals*, 23,
732 452-460.
733
- 734 Ibberson, R.M., David, W.I.F. and Knight, K.S. (1992) The high resolution neutron powder
735 diffractometer (HRPD) at ISIS - A user guide. Report RAL-92-031.
736
- 737 Ihinger, P.D. and Stolper, E. (1986) The color of meteoritic hibonite: an indicator of oxygen
738 fugacity. *Earth and Planetary Science Letters*, 78, 67-79.
739
- 740 Ireland, T.R. (1988) Correlated morphological, chemical, and isotopic characteristics of hibonites
741 from the Murchison carbonaceous chondrite. *Geochimica et Cosmochimica Acta* 52, 2827-2839.
742
- 743 Iyi, N., Takekawa, S. and Kimura, S. (1989) Crystal chemistry of hexaaluminates: β -alumina and
744 magnetoplumbite structures. *Journal of Solid State Chemistry*, 83, 8-19.
745

- 746 Junquera, J., Paz, O., Sánchez-Portal, D. and Artacho, E. (2001) Numerical atomic orbitals for
747 linear-scaling calculations. *Physical Review B*, 64, art. no. 235111.
748 doi:10.1103/PhysRevB.64.235111.
749
- 750 Kato, K. and Saalfeld, H. (1968) Verfeinerung der Kristallstruktur von $\text{CaO} \cdot 6\text{Al}_2\text{O}_3$. *Neues*
751 *Jahrbuch für Mineralogie, Abhandlungen*, 109, 192-200.
752
- 753 Kohn, J.A. and Eckart, D.W. (1964) New hexagonal ferrite, establishing a second structural series.
754 *Journal of Applied Physics*, 35, 968-969.
755
- 756 Kohn, W. and Sham, L.J. (1965) Self-consistent equations including exchange and correlation
757 effects. *Physical Review*, 140, 1133-1138.
758
- 759 Kreber, E.E. and Gonser, U.U. (1976) Determination of cation distribution in Ti^{4+} and Co^{2+}
760 substituted barium ferrite by Mössbauer spectroscopy. *Applied Physics*, 10, 175-180.
761
- 762 Krot, A.N., Fagan, T.J., Keil, K., McKeegan, K.D., Sahijpal, S., Hutcheon, I.D., Petaev, M.I. and
763 Yurimoto, H. (2004) Ca, Al-rich inclusions, amoeboid olivine aggregates, and Al-rich chondrules
764 from the unique carbonaceous chondrite Acfer 094: I. mineralogy and petrology. *Geochimica et*
765 *Cosmochimica Acta*, 68, 2167-2184.
766
- 767 Krot, A., McKeegan, K., Huss, G., Liffman, K., Sahijpal, S. and Hutcheon, I. (2006) Aluminium-
768 magnesium and oxygen isotope study of relict Ca-Al-rich inclusions in chondrules. *Astrophysical*
769 *Journal*, 639, 1227-1237
770
- 771 Larson, A.C. and Von Dreele, R.B. (1994) General Structure Analysis System (GSAS), Los Alamos
772 National Laboratory Report. LAUR 86-748 (revised version).
773
- 774 Leslie, M. and Gillan, M.J. (1985) The energy and elastic dipole tensor of defects in ionic crystals
775 calculated by the supercell method. *Journal of Physics C: Solid State Physics*, 18, 973-982.
776
- 777 Lodders, K. (2003) Solar System abundances and condensation temperatures of the elements.
778 *Astrophysical Journal*, 591, 1220-1247.
779
- 780 Nagashima, M., Armbruster, T. and Hainschwang, T. (2010) A temperature-dependent structure

- 781 study of gem-quality hibonite from Myanmar. *Mineralogical Magazine*, 74, 871-885.
782
- 783 Paglia, G., Rohl, A.L., Buckley, C.E. and Gale, J.D. (2005) Determination of the structure of γ -
784 alumina from interatomic potential and first-principles calculations: The requirement of significant
785 numbers of nonspinel positions to achieve an accurate structural model. *Physical Review B*, 71 art.
786 no. 224115. doi:10.1103/PhysRevB.71.224115.
787
- 788 Palin, E.J., Walker, A.M. and Harrison, R.J. (2008) A computational study of order-disorder
789 phenomena in Mg_2TiO_4 spinel (qandilite). *American Mineralogist*, 93, 1363-1372.
790 doi:10.2138/am.2008.2896.
791
- 792 Perdew, J.P., Burke, K. and Emzerhof, M. (1996) Generalized gradient approximation made simple.
793 *Physical Review Letters*, 77, 3865–3868.
794
- 795 Rager, H., Geiger, C.A. and Stahl, A. (2003) Ti(III) in synthetic pyrope: A single-crystal electron
796 paramagnetic resonance study. *European Journal of Mineralogy*, 15, 697-699.
797
- 798 Rakotondrazafy, M.A.F., Moine, B. and Cuney, M. (1996) Mode of formation of hibonite
799 ($\text{CaAl}_{12}\text{O}_{19}$) within the U-Th skarns from the granulites of S-E Madagascar. *Contributions to*
800 *Mineralogy and Petrology*, 123, 190-201.
801
- 802 Rietveld, H.M. (1969) A profile refinement method for nuclear and magnetic structures. *Journal of*
803 *Applied Crystallography*, 2, 65-71.
804
- 805 Rietveld, H.M. (2000) The early days: a retrospective view, in Young, R.A. ed., *The Rietveld*
806 *Method*: Oxford University Press, 39-42.
807
- 808 Rout, S.S. and Bischoff, A. (2008) Ca, Al-rich inclusions in Rumurud (R) chondrites. *Meteoritics*
809 *and Planetary Science*, 43, 1439-1464.
810
- 811 Rout, S.S., Bischoff, A., Nagashima, K., Krot, A.N., Huss, G.R. and Keil, K. (2009) Oxygen- and
812 magnesium-isotope compositions of calcium-aluminum-rich inclusions from Rumuruti (R)
813 chondrites. *Geochimica et Cosmochimica Acta*, 73, 4264-4287.
814

- 815 Sanchez, A., Strauss, A.J., Aggarwal, R.L. and Fahey, R.E. (1988) Crystal-growth, spectroscopy,
816 and laser characteristics of Ti-Al₂O₃. IEEE Journal of Quantum Electronics, 24, 955-1002.
817
- 818 Schofield, P.F., Knight, K.S., Covey-Crump, S.J., Cressey, G. and Stretton, I.C. (2002) Accurate
819 quantification of the modal mineralogy of rocks when image analysis is difficult. Mineralogical
820 Magazine, 66, 189–200.
821
- 822 Schofield, P.F., Smith, A.D., Mosselmans, J.F.W., Ohldag, H., Scholl, A., Raoux, S., Cressey, G.,
823 Cressey, B.A., Quinn, P.D., Kirk, C.A. and Hogg, S.C. (2010) X-ray spectromicroscopy of mineral
824 intergrowths in the Santa Catharina meteorite. Geostandards and Geoanalytical Research, 34, 145-
825 159.
826
- 827 Sears, V.F. (1992) Neutron scattering lengths and cross sections. Neutron News, 3, 26-37.
828
- 829 Shannon, R.D. (1976) Revised effective ionic radii and systematic studies of interatomic distances
830 in halides and chalcogenides. Acta Crystallographica, A32, 751-767.
831
- 832 Simon, S.B., Sutton, S.R. and Grossman, L. (2007) Valence of titanium and vanadium in pyroxene
833 in refractory inclusion interiors and rims. Geochimica et Cosmochimica Acta, 71, 3098-3118.
834
- 835 Smith, A.D., Schofield, P.F., Cressey, G., Cressey, B.A. and Read, P.D. (2004) The development of
836 X-ray photo-emission electron microscopy (XPEEM) for valence-state imaging of mineral
837 intergrowths. Mineralogical Magazine, 68, 859–869.
838
- 839 Soler, J.M., Artacho, E., Gale, J.D., García, A., Junquera, J., Ordejón, P. and Sánchez-Portal, D.
840 (2002) The SIESTA method for ab initio order-N materials simulation. Journal of Physics
841 Condensed Matter, 14, 2745–2776.
842
- 843 Tailby, N.D., Walker, A.M., Berry, A.J., Hermann, J., Evans, K.A., Mavrogenes, J.A., O'Neill,
844 H.St.C., Rodina, I.S., Soldatov, A.V., Rubatto, D. and Sutton, S.R. (2011) Ti site occupancy in
845 zircon. Geochimica et Cosmochimica Acta, 75, 905-921. doi:10.1016/j.gca.2010.11.004.
846
- 847 Toby, B.H. (2001) EXPGUI, a graphical user interface for GSAS. Journal of Applied
848 Crystallography, 34, 210-221.
849

- 850 Ushikubo, T., Hiyagon, H. and Sugiura, N. (2007) A FUN-like hibonite inclusion with a large
851 ²⁶Mg-excess. *Earth and Planetary Science Letters*, 254, 115-126.
852
- 853 Utsunomiya, A.A., Tanaka, K., Morikawa, H., Marumo, F. and Kojima, H. (1988) Structure
854 refinement of CaO.6Al₂O₃. *Journal of Solid State Chemistry*, 75, 197-200.
855
- 856 Vázquez, B.A., Caballero, A. and Pena, P. (2003) Quaternary system Al₂O₃-MgO-SiO₂: I, Study of
857 the crystallization volume of Al₂O₃. *Journal of the American Ceramic Society*, 86, 2195-2199.
858
- 859 Walker, A.M., Hermann, J., Berry, A.J. and O'Neill, H.St.C. (2007) Three water sites in upper
860 mantle olivine and the role of titanium in the water weakening mechanism. *Journal of Geophysical*
861 *Research*, 112, art. no. B05211. doi:10.1029/2006JB004620.
862
- 863 Warren, M.C., Dove, M.T., Myers, E.R., Bosenick, A., Palin, E.J., Sainz-Diaz, C.I., Guiton, B.S.
864 and Redfern, S.A.T. (2001) Monte Carlo methods for the study of cation ordering in minerals.
865 *Mineralogical Magazine*, 65, 221–248.
866
- 867 Weber, D. and Bischoff, A. (1994) The occurrence of grossite (CaAl₄O₇) in chondrites. *Geochimica*
868 *et Cosmochimica Acta*, 58, 3855-3877.
869
- 870 Wittmann, A., Seifert, K. and Nowotny, H. (1958) Ein Beitrag zum Aufbau des Kalzium-Titan(III)-
871 Aluminats. *Monatshefte für Chemie*, 89, 225-228.
872
- 873 Woodley, S.M., Gale, J.D., Battle, P.D. and Catlow, C.R.A. (2003) Oxygen ion migration in
874 orthorhombic LaMnO_{3-δ}. *Journal of Chemical Physics*. 119, 9737-9744.
875
- 876 Yamaga, M., Yosida, T., Hara, S., Kodama, N. and Henderson, B. (1994) Optical and electron spin
877 resonance spectroscopy of Ti³⁺ and Ti⁴⁺ in Al₂O₃. *Journal of Applied Physics*, 75, 1111-1117.
878
- 879 Yoneda, S. and Grossman, L. (1995) Condensation of CaO-MgO-Al₂O₃-SiO₂ liquids from cosmic
880 gases. *Geochimica et Cosmochimica Acta*, 59, 3413-3444.
881
- 882 Young, R.A. (1993) Introduction to the Rietveld method, in Young, R.A. ed., *The Rietveld Method*:
883 Oxford University Press, Oxford, pp. 1-38.
884

885

List of Figures

886 **Figure 1.** The two structural layers, R-block and S-block, of hibonite with the *c* axis vertical, shown
887 as a composite of both ball-and-stick and polyhedral representations. The R-block comprises the
888 Ca site, the trigonal bipyramidal M2 site and the octahedral face-sharing M4 site. The S-block
889 comprises layers of M5 octahedra interspersed with a layer containing the M3 tetrahedra and the
890 M1 octahedra.

891

892 **Figure 2.** Ti per formula unit (pfu) against Mg pfu for the synthetic samples of this study and
893 meteoritic hibonite. The meteoritic data are from Fuchs et al. (1973), Allen et al. (1978),
894 Armstrong et al. (1982), Davis et al. (1982), Burns and Burns (1984), Ireland (1988), Weber and
895 Bischoff (1994), Bischoff and Srinivasan (2003), Krot et al. (2004), Krot et al. (2006), Ushikubo et
896 al. (2007), Rout et al. (2009), and Doyle (2012).

897

898 **Figure 3.** Observed, calculated and difference profiles for (a) the Ti^{3+} end-member hibonite
899 (0.20,1.0) and (b) the Ti^{4+} end-member hibonite (0.98,0). The dots represent the observed data and
900 the solid lines the calculated profiles.

901

902 **Figure 4.** Ti and Mg pfu of the synthetic hibonite samples determined from Rietveld refinement
903 and energy dispersive spectrometry (EDS).

904

905 **Figure 5.** The occupancy of Ti^{4+} as a fraction of 1 on (a) M2 and (b) M4 as a function of Ti^{4+} pfu.

906

907 **Figure 6.** Unit-cell parameters of Ti-bearing hibonite samples as a function of Ti pfu derived from
908 the Rietveld refinements (solid symbols). (a) *a* cell parameter, (b) *c* cell parameter and (c) *c/a* ratio.
909 The values for $CaAl_{12}O_{19}$, terrestrial Ti^{4+} hibonite (open circle) and synthetic $CaAl_{10.1}Ti_{1.9}O_{19}$ (open
910 square) are taken from Hofmeister et al. (2004), Nagashima et al. (2010) and Wittmann et al. (1958)
911 respectively. For Figures 6-11, where error bars are not visible then symbols are larger than the
912 errors.

913

914 **Figure 7.** Unit-cell parameters of Ti-bearing hibonite samples as a function of Ti^{4+} pfu. (a) *a* cell
915 parameter and (b) *c* cell parameter.

916

917 **Figure 8.** The (a) M3-O2 and (b) M3-O4 distances as a function of Ti^{4+} pfu.

918

919 **Figure 9.** The (a) M5-O1, (b) M5-O2, (c) M5-O4 and (d) M5-O5 distances as a function of Ti^{4+}

920 pfu.

921

922 **Figure 10.** The axial (a) M2-O1a and (b) M2-O1b distances as a function of Ti pfu and (c) the M2-
923 O1a distance as a function of Ti^{4+} pfu.

924

925 **Figure 11.** The (a) M4-M4, (b) M4-O3 and (c) M4-O5 distances as a function of Ti pfu.

926

927 **Table 1** Substitution sites of selected cations in natural and synthetic hibonite and various structural
 928 analogues.

Site	Hibonite ^{1,2,3,4,5}	Magnetoplumbite ^{3,6}	β , β'' alumina ^{7,8}	Sr Y ₁₂ O ₁₉ ^{9,10}	Ba Y ₁₂ O ₁₉ ¹¹
M1	Cr ³⁺	Al ³⁺ Cr ³⁺	Al ³⁺ Ti ³⁺	Cr ³⁺ Ti ⁴⁺	Fe ³⁺ Ti ⁴⁺
M2	Fe ²⁺ Fe ³⁺ V ³⁺ Ti ³⁺ Ti ⁴⁺	Mn ⁴⁺ Fe ³⁺	Al ³⁺	Co ²⁺ Ti ⁴⁺ Ga ³⁺	Fe ³⁺ Co ²⁺ Ti ⁴⁺
M3	Mg ²⁺ Fe ²⁺ Fe ³⁺ Zn ²⁺ Si ⁴⁺	Mn ²⁺ Zn ²⁺ Fe ³⁺ Fe ²⁺ Mg ²⁺	Al ³⁺ Mg ²⁺	Co ²⁺ Ga ³⁺	Fe ³⁺ Co ²⁺
M4	Fe ²⁺ Cr ³⁺ Ti ⁴⁺ Si ⁴⁺	Fe ³⁺ Mn ⁴⁺ Sb ⁵⁺ Ti ⁴⁺	Al ³⁺	Cr ³⁺ Ti ⁴⁺	Fe ³⁺ Ti ⁴⁺
M5	Cr ³⁺	Al ³⁺ Mn ³⁺ Cr ³⁺ Fe ³⁺ Ti ⁴⁺	Al ³⁺ Ti ³⁺	Cr ³⁺ Ti ⁴⁺ Co ²⁺	Fe ³⁺ Co ²⁺ Ti ⁴⁺

929 References: (1) Burns and Burns (1984); (2) Beckett et al. (1988); (3) Bermanec et al. (1996); (4) Holtstam (1996); (5)
 930 Nagashima et al. (2010); (6) Grey et al. (1987); (7) Bettman and Peters (1969); (8) Barret et al. (1985); (9) Graetsch and
 931 Gebert (1995); (10) Graetsch and Gebert (1996); (11) Kreber and Gonsler (1976)

932 **Table 2** Chemical composition of synthetic hibonite samples determined by energy dispersive X-ray spectrometry (EDS). The sample nomenclature is of the form
 933 (Ti pfu, Ti³⁺/ΣTi). Secondary phases are those identified by NPD and are less than 3 wt%. Standard deviations are in parentheses.

934

Sample	No. analyses	CaO	Al ₂ O ₃	MgO	TiO ₂ *	Total	Stoichiometry	Secondary phases
(0.20,1.0)	37	8.8 (0.4)	88.2 (0.6)	-	2.4 (0.5)	99.4 (0.7)	Ca _{1.07} Al _{11.69} Ti _{0.20} O ₁₉	Al ₂ O ₃
(0.33,1.0)	30	8.8 (0.3)	86.7 (0.6)	-	4.0 (0.4)	99.5 (0.8)	Ca _{1.07} Al _{11.51} Ti _{0.33} O ₁₉	Al ₂ O ₃
(0.62,0.60)	27	8.7 (0.3)	82.8 (0.5)	1.5 (0.1)	7.3 (0.5)	100.2 (0.7)	Ca _{1.05} Al _{10.99} Ti _{0.62} Mg _{0.24} O ₁₉	-
(0.73,0.33)	42	8.8 (0.3)	79.9 (1.0)	2.9 (0.2)	8.6 (0.7)	100.2 (0.9)	Ca _{1.07} Al _{10.66} Ti _{0.73} Mg _{0.49} O ₁₉	Al ₂ O ₃
(0.82,0.27)	41	8.6 (0.3)	78.6 (2.5)	3.5 (0.6)	9.6 (2.2)	100.3 (0.9)	Ca _{1.05} Al _{10.48} Ti _{0.82} Mg _{0.60} O ₁₉	MgAl ₂ O ₃
(1.37,0.39)	18	8.6 (0.3)	71.0 (1.1)	4.9 (0.2)	15.9 (0.9)	100.4 (0.8)	Ca _{1.05} Al _{9.59} Ti _{1.37} Mg _{0.83} O ₁₉	MgAl ₂ O ₃ , Ti ₂ O ₃
(0.44,0)	26	8.5 (0.3)	83.0 (1.9)	2.5 (0.6)	5.2 (1.4)	99.2 (0.6)	Ca _{1.04} Al _{11.10} Ti _{0.44} Mg _{0.43} O ₁₉	MgAl ₂ O ₃
(0.98,0)	28	8.3 (0.4)	74.8 (0.7)	5.4 (0.2)	11.4 (0.7)	100.0 (0.9)	Ca _{1.01} Al _{10.07} Ti _{0.98} Mg _{0.91} O ₁₉	MgAl ₂ O ₃ , CaTiO ₃

935 * Ti as TiO₂

936

937

938

939

940

941

942

943

944

945

946

947

948

949 **Table 3** Lattice parameters and Mg and Ti site occupancies (as fractions of 1) derived from the Rietveld refinements. The occupancies of Ti³⁺ and Ti⁴⁺ on M4
950 were calculated assuming that Ti⁴⁺ pfu = Mg²⁺ pfu, Ti³⁺ only occupies M4 and all the Ti on M2 is Ti⁴⁺.

951

Sample	a (Å)	c (Å)	Volume (Å ³)	Mg on M3	Ti on M2*	Ti on M4	Ti ³⁺ on M4	Ti ⁴⁺ on M4	Ti ⁴⁺ M2/M4 †
(0.20,1.0)	5.567260 (6)	21.92612 (4)	588.539 (1)	-	-	0.096 (1)	0.096 (1)	-	-
(0.33,1.0)	5.570159 (9)	21.93871 (6)	589.491 (2)	-	-	0.144 (1)	0.144 (1)	-	-
(0.62,0.60)	5.586154 (7)	21.98939 (5)	594.251 (1)	0.12 (1)	0.020 (5)	0.250 (5)	0.15 (1)	0.10 (1)	0.20 (1)
(0.73,0.33)	5.596009 (8)	22.01478 (5)	597.038 (1)	0.26 (1)	0.040 (5)	0.310 (5)	0.09 (1)	0.22 (1)	0.18 (1)
(0.82,0.27)	5.603373 (9)	22.03238 (6)	599.089 (2)	0.33 (1)	0.065 (3)	0.360 (5)	0.09 (1)	0.27 (1)	0.24 (1)
(1.37,0.39)	5.62894 (1)	22.12121 (7)	607.006 (2)	0.42 (1)	0.050 (5)	0.600 (5)	0.23 (1)	0.37 (1)	0.14 (1)
(0.44,0)	5.58641 (1)	21.99031 (8)	594.329 (4)	0.21 (1)	0.030 (5)	0.190 (5)	-	0.190 (5)	0.16 (1)
(0.98,0)	5.607263 (7)	22.07468 (5)	601.072 (1)	0.46 (1)	0.065 (3)	0.403 (3)	-	0.403 (5)	0.16 (1)

952

* Site is half occupied.

953

† For the hibonite structure M2/M4 calculated in terms of occupancy is equivalent to M2/M4 pfu.

954

955

956 **Table 4** Atomic coordinates and isotropic displacement parameters ($U_{\text{iso}} \times 100$).

957

		(0.20,1.0)	(0.33,1.0)	(0.62,0.60)	(0.73,0.33)	(0.82,0.27)	(1.37,0.39)	(0.44,0)	(0.98,0)
Ca	x	0.6667	0.6667	0.6667	0.6667	0.6667	0.6667	0.6667	0.6667
	y	0.3333	0.3333	0.3333	0.3333	0.3333	0.3333	0.3333	0.3333
	z	0.2500	0.2500	0.2500	0.2500	0.2500	0.2500	0.2500	0.2500
	U_{iso}	1.14(3)	0.99(5)	2.09(3)	2.03(3)	2.04(4)	3.03(1)	3.15(1)	2.77(4)
M1	x	0	0	0	0	0	0	0	0
	y	0	0	0	0	0	0	0	0
	z	0	0	0	0	0	0	0	0
	U_{iso}	0.73(3)	1.11(5)	0.89(3)	0.82(3)	0.76(4)	0.71(1)	1.06(1)	0.88(4)
M2	x	0	0	0	0	0	0	0	0
	y	0	0	0	0	0	0	0	0
	z	0.2591(1)	0.2598(2)	0.2621(1)	0.2620(1)	0.2620(2)	0.2657(1)	0.2612(1)	0.2641(1)
	U_{iso}	1.71(5)	1.84(8)	2.02(6)	1.92(7)	2.03(9)	1.75(1)	2.02(1)	1.90(4)
M3	x	0.3333	0.3333	0.3333	0.3333	0.3333	0.3333	0.3333	0.3333
	y	0.6667	0.6667	0.6667	0.6667	0.6667	0.6667	0.6667	0.6667
	z	0.02781(5)	0.02878(7)	0.02849(4)	0.02821(4)	0.02861(4)	0.02921(1)	0.02701(1)	0.02791(6)
	U_{iso}	1.07(2)	1.37(3)	1.23(2)	1.15(2)	1.09(2)	0.88(1)	1.17(1)	1.32(4)
M4	x	0.3333	0.3333	0.3333	0.3333	0.3333	0.3333	0.3333	0.3333
	y	0.6667	0.6667	0.6667	0.6667	0.6667	0.6667	0.6667	0.6667
	z	0.19044(5)	0.19029(9)	0.18900(8)	0.1879(1)	0.1875(2)	0.18789(9)	0.1901(1)	0.1865(1)
	U_{iso}	0.65(5)	0.80(9)	1.28(5)	1.07(7)	1.2(1)	1.07(1)	1.13(1)	1.23(4)
M5	x	0.16863(7)	0.1693(1)	0.16908(7)	0.16870(7)	0.16902(9)	0.16774(4)	0.16855(3)	0.16872(2)
	y	0.3372(1)	0.3384(2)	0.3380(1)	0.3373(1)	0.3379(2)	0.3354(1)	0.3371(1)	0.33732(4)
	z	-0.10904(2)	-0.10883(2)	-0.10846(2)	-0.10809(2)	-0.10786(2)	-0.10651(1)	-0.10894(1)	-0.10731(6)
	U_{iso}	1.04(1)	1.30(2)	1.38(1)	1.28(1)	1.27(1)	1.21(1)	1.20(1)	1.40(4)
O1	x	0	0	0	0	0	0	0	0
	y	0	0	0	0	0	0	0	0
	z	-0.14940(3)	-0.14985(4)	-0.14960(3)	-0.15003(3)	-0.15054(4)	-0.14927(1)	-0.15001(8)	-0.15037(6)
	U_{iso}	0.72(2)	1.20(3)	1.27(2)	0.76(2)	0.65(3)	0.66(1)	1.54(1)	1.29(4)
O2	x	0.6667	0.6667	0.6667	0.6667	0.6667	0.6667	0.6667	0.6667
	y	0.3333	0.3333	0.3333	0.3333	0.3333	0.3333	0.3333	0.3333
	z	0.05403(3)	0.05280(6)	0.05458(3)	0.05542(3)	0.05593(4)	0.05668(1)	0.05597(1)	0.05753(6)
	U_{iso}	0.88(2)	0.89(2)	1.17(2)	1.25(2)	1.14(2)	1.38(1)	1.18(5)	1.30(4)
O3	x	0.18166(6)	0.1817(1)	0.18033(6)	0.18049(6)	0.18094(7)	0.17842(4)	0.17986(3)	0.18101(2)
	y	0.3634(1)	0.3635(2)	0.3608(1)	0.3611(1)	0.3620(1)	0.3570(1)	0.3598(1)	0.3621(1)
	z	0.2500	0.2500	0.2500	0.2500	0.2500	0.2500	0.2500	0.2500
	U_{iso}	1.24(1)	1.70(2)	1.67(1)	1.65(1)	1.58(2)	1.09(1)	1.48(1)	1.58(4)
O4	x	0.15600(4)	0.15542(6)	0.15465(3)	0.15400(4)	0.15341(4)	0.15303(4)	0.15398(3)	0.15251(2)
	y	0.31200(8)	0.3108(1)	0.30931(7)	0.30801(7)	0.30682(8)	0.30608(8)	0.30797(7)	0.30502(4)
	z	0.05210(1)	0.05261(2)	0.05238(1)	0.05278(1)	0.05300(2)	0.05329(1)	0.05263(1)	0.05332(1)
	U_{iso}	0.97(1)	1.27(1)	1.37(1)	1.34(1)	1.34(1)	0.86(1)	1.24(1)	1.48(4)
O5	x	0.50357(5)	0.50303(8)	0.50412(4)	0.50455(4)	0.50469(5)	0.50609(4)	0.50367(3)	0.50419(2)
	y	1.0072(1)	1.0061(2)	1.00833(8)	1.00918(8)	1.0095(1)	1.01225(8)	1.00743(7)	1.00846(4)
	z	0.14899(1)	0.14887(1)	0.14893(1)	0.14935(1)	0.14934(2)	0.14949(1)	0.14922(1)	0.14978(1)
	U_{iso}	1.00(1)	1.27(1)	1.32(1)	1.35(1)	1.29(1)	0.75(1)	1.13(1)	1.26(4)

958

959

960 **Table 5** Energies of isolated defects at 0 K.

961

Defect (Kröger-Vink notation)	Energy (eV / 256 atom cell)	Notes
No defect	-88959.2740	CaAl ₁₂ O ₁₉ hibonite, 256 atoms
Ti _{Al(1)} ^x	-90393.3591	Ti ³⁺ on M1
Ti _{Al(2)} ^x	-90394.1357	Ti ³⁺ on M2
Ti _{Al(3)} ^x	-90393.8763	Ti ³⁺ on M3
Ti _{Al(4)} ^x	-90393.8734	Ti ³⁺ on M4
Ti _{Al(5)} ^x	-90393.7426	Ti ³⁺ on M5
Ti _{Al(1)} [•]	-90387.3766	Ti ⁴⁺ on M1
Ti _{Al(2)} [•]	-90389.3807	Ti ⁴⁺ on M2
Ti _{Al(3)} [•]	-90387.9251	Ti ⁴⁺ on M3
Ti _{Al(4)} [•]	-90389.0742	Ti ⁴⁺ on M4
Ti _{Al(5)} [•]	-90388.5411	Ti ⁴⁺ on M5
Mg _{Al(1)} [']	-89836.9945	Mg ²⁺ on M1
Mg _{Al(2)} [']	-89836.2080	Mg ²⁺ on M2
Mg _{Al(3)} [']	-89837.8229	Mg ²⁺ on M3
Mg _{Al(4)} [']	-89836.0045	Mg ²⁺ on M4
Mg _{Al(5)} [']	-89836.6277	Mg ²⁺ on M5

962

963

964

965

966

967 **Table 6** Energies of clustered defect structures including Ti-Mg and Ti-Ti interactions at 0 K. Defects
 968 labeled with (a) and (b) subscripts occur as multiple symmetrically distinct clusters, which can be
 969 distinguished using the Ti-Mg distances.

Defect (Kröger-Vink notation)	Energy (eV / 256 atom cell)	Ti-Mg distance (Å)	Notes
No defect	-88959.2740	-	CaAl ₁₂ O ₁₉ hibonite, 256 atoms
{Ti _{Al(1)} ·Mg _{Al(3)} '}	-91267.2759	3.30	Ti ⁴⁺ and Mg ²⁺ on M1 and M3
{Ti _{Al(1)} ·Mg _{Al(5)} '}	-91266.0809	2.19	Ti ⁴⁺ and Mg ²⁺ on M1 and M5
{Ti _{Al(2)} ·Mg _{Al(4)} '}(a)	-91267.5971	3.45	Ti ⁴⁺ and Mg ²⁺ on M2 and M4
{Ti _{Al(2)} ·Mg _{Al(4)} '}(b)	-91267.6954	3.54	Ti ⁴⁺ and Mg ²⁺ on M2 and M4
{Ti _{Al(2)} ·Mg _{Al(5)} '}(a)	-91268.1237	3.40	Ti ⁴⁺ and Mg ²⁺ on M2 and M5
{Ti _{Al(2)} ·Mg _{Al(5)} '}(b)	-91268.1161	3.61	Ti ⁴⁺ and Mg ²⁺ on M2 and M5
{Ti _{Al(3)} ·Mg _{Al(1)} '}	-91266.9784	3.30	Ti ⁴⁺ and Mg ²⁺ on M3 and M1
{Ti _{Al(3)} ·Mg _{Al(5)} '}(a)	-91266.4905	3.44	Ti ⁴⁺ and Mg ²⁺ on M3 and M5
{Ti _{Al(3)} ·Mg _{Al(5)} '}(b)	-91267.1033	3.33	Ti ⁴⁺ and Mg ²⁺ on M3 and M5
{Ti _{Al(4)} ·Mg _{Al(5)} '}	-91267.8774	3.33	Ti ⁴⁺ and Mg ²⁺ on M4 and M5
{Ti _{Al(4)} ·Mg _{Al(4)} '}	-91267.5227	2.60	Ti ⁴⁺ and Mg ²⁺ on M4 and M4
{Ti _{Al(4)} ·Mg _{Al(2)} '}(a)	-91267.5280	3.45	Ti ⁴⁺ and Mg ²⁺ on M4 and M2
{Ti _{Al(4)} ·Mg _{Al(2)} '}(b)	-91267.5610	3.54	Ti ⁴⁺ and Mg ²⁺ on M4 and M2
{Ti _{Al(5)} ·Mg _{Al(5)} '}(a)	-91267.2759	2.77	Ti ⁴⁺ and Mg ²⁺ on M5 and M5
{Ti _{Al(5)} ·Mg _{Al(5)} '}(b)	-91267.5073	2.84	Ti ⁴⁺ and Mg ²⁺ on M5 and M5
{Ti _{Al(5)} ·Mg _{Al(4)} '}	-91266.9258	3.33	Ti ⁴⁺ and Mg ²⁺ on M5 and M4
{Ti _{Al(5)} ·Mg _{Al(2)} '}(a)	-91266.8811	3.40	Ti ⁴⁺ and Mg ²⁺ on M5 and M2
{Ti _{Al(5)} ·Mg _{Al(2)} '}(b)	-91266.8884	3.61	Ti ⁴⁺ and Mg ²⁺ on M5 and M2
{Ti _{Al(5)} ·Mg _{Al(1)} '}	-91267.5402	2.91	Ti ⁴⁺ and Mg ²⁺ on M5 and M1
{Ti _{Al(5)} ·Mg _{Al(3)} '}(a)	-91268.3199	3.43	Ti ⁴⁺ and Mg ²⁺ on M5 and M3
{Ti _{Al(5)} ·Mg _{Al(3)} '}(b)	-91268.3299	3.32	Ti ⁴⁺ and Mg ²⁺ on M5 and M3
{Ti _{Al(2)} ·Mg _{Al(3)} '}(a)	-91269.1850	5.76	Ti ⁴⁺ and Mg ²⁺ on M2 and M3
{Ti _{Al(2)} ·Mg _{Al(3)} '}(b)	-91269.2066	5.97	Ti ⁴⁺ and Mg ²⁺ on M2 and M3
{Ti _{Al(4)} ·Mg _{Al(3)} '}	-91268.8648	3.59	Ti ⁴⁺ and Mg ²⁺ on M4 and M3
{Ti _{Al(4)} ^x Ti _{Al(4)} ^x }	-91830.7191	-	Ti ³⁺ on M4
{Ti _{Al(4)} ·Ti _{Al(4)} ·Mg _{Al(3)} 'Mg _{Al(3)} '}	-93579.4590	3.51 and 3.53	Ti ⁴⁺ and Mg ²⁺ on M4 and M3

970

971

972 **Table 7** Selected interatomic distances (Å); R = R-block, S = S-block.

973

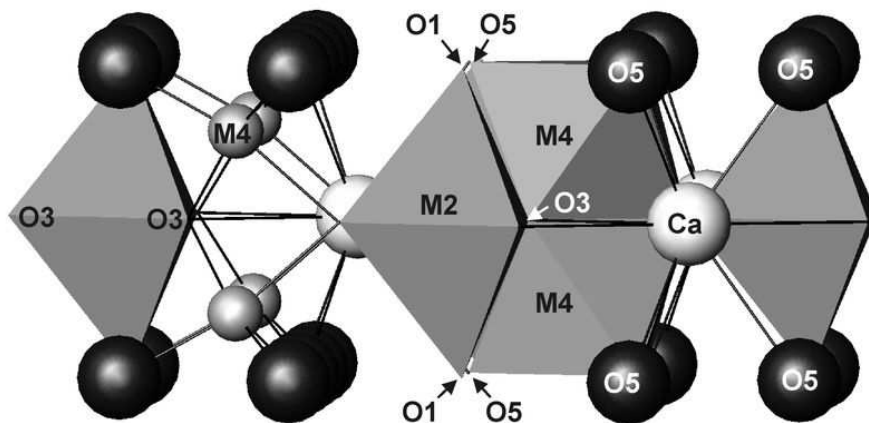
	(0.20,1.0)	(0.33,1.0)	(0.62,0.60)	(0.73,0.33)	(0.82,0.27)	(1.37,0.39)	(0.44,0)	(0.98,0)
Ca-O3 (×6)	2.78798(3)	2.78945(5)	2.79681(3)	2.80182(3)	2.80573(3)	2.81742(4)	2.79673(2)	2.80769(1)
Ca-O5 (×6)	2.7160(3)	2.7228(5)	2.7224(3)	2.7161(3)	2.7181(4)	2.7190(6)	2.7197(2)	2.7171(2)
M1-O4 (×6)	1.8889(4)	1.8921(6)	1.8883(3)	1.8916(3)	1.8923(4)	1.9016(6)	1.8866(3)	1.8920(2)
M2-O1 _a	2.006(3)	1.983(4)	1.941(2)	1.937(3)	1.926(4)	1.881(4)	1.951(1)	1.888(3)
M2-O1 _b	2.406(3)	2.411(4)	2.474(2)	2.465(3)	2.457(4)	2.575(3)	2.447(3)	2.510(3)
M2-O3 (×3)	1.7636(7)	1.766(1)	1.7655(6)	1.7697(7)	1.7765(9)	1.7744(8)	1.7584(3)	1.7857(2)
M3-O2	1.794(1)	1.790(2)	1.8266(9)	1.8411(9)	1.863(1)	1.8998(8)	1.8247(3)	1.8859(3)
M3-O4 (×3)	1.7912(5)	1.7945(7)	1.8070(4)	1.8205(4)	1.8272(5)	1.8369(8)	1.8247(3)	1.8438(4)
M4-O3 (×3)	1.9605(8)	1.964(2)	1.997(1)	2.016(2)	2.021(3)	2.0416(6)	1.985(1)	2.038(2)
M4-O5 (×3)	1.8766(6)	1.873(1)	1.8730(9)	1.864(1)	1.864(2)	1.8865(6)	1.877(1)	1.8471(2)
M5-O1	1.8509(7)	1.864(1)	1.8689(7)	1.8774(8)	1.890(1)	1.8887(8)	1.8643(3)	1.8939(2)
M5-O2	1.9948(8)	2.005(1)	1.9828(7)	1.9730(8)	1.963(1)	1.9555(8)	1.9747(3)	1.9407(3)
M5-O4 (×2)	2.0044(4)	1.9965(7)	1.9970(5)	1.9854(5)	1.9809(6)	1.9609(8)	1.9959(3)	1.9673(4)
M5-O5 (×2)	1.8075(5)	1.8089(7)	1.8148(4)	1.8261(5)	1.8288(6)	1.8527(8)	1.8165(3)	1.8450(4)
M4-M4	2.612(2)	2.620(4)	2.683(4)	2.734(5)	2.754(8)	2.748(4)	2.635(3)	2.803(3)
O1-O1 (R)	4.412(1)	4.394(2)	4.415(1)	4.402(1)	4.383(2)	4.456(4)	4.398(1)	4.398(3)
O1-O1 (S)	6.551(1)	6.575(2)	6.579(1)	6.606(1)	6.634(2)	6.604(4)	6.598(3)	6.639(3)

974

975

976

R-block



S-block

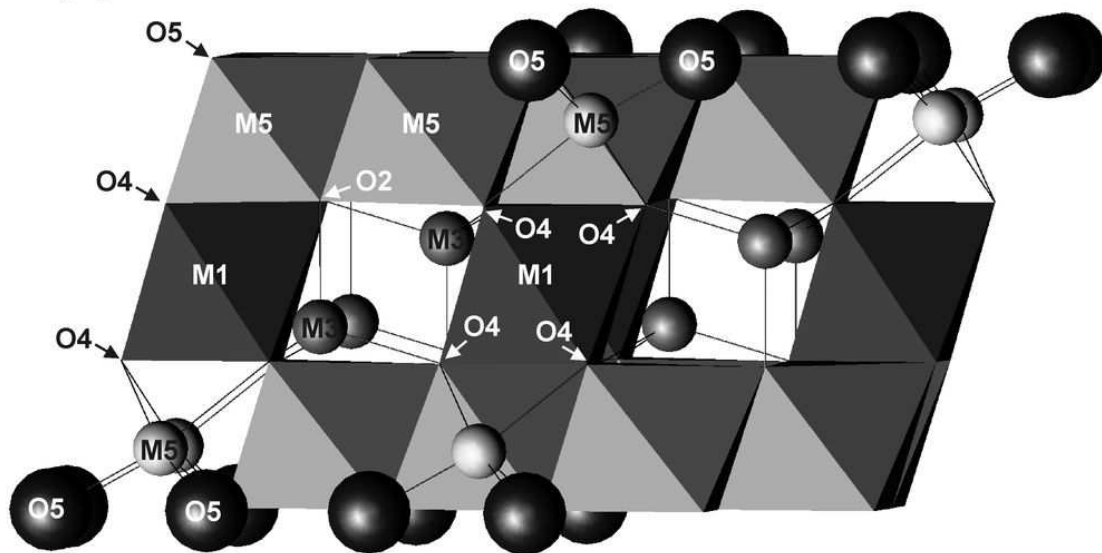


Figure 2 Doyle et al 2013

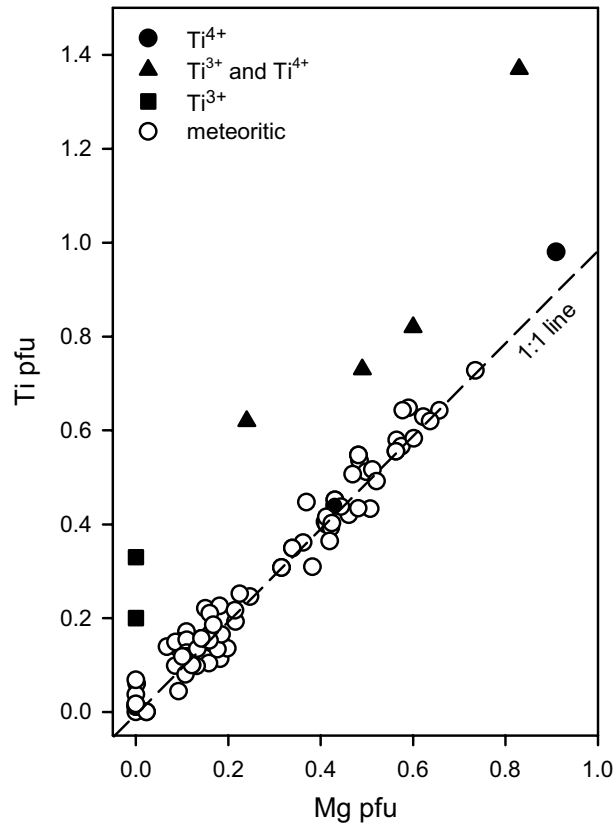


Figure 3 Doyle et al. (2013)

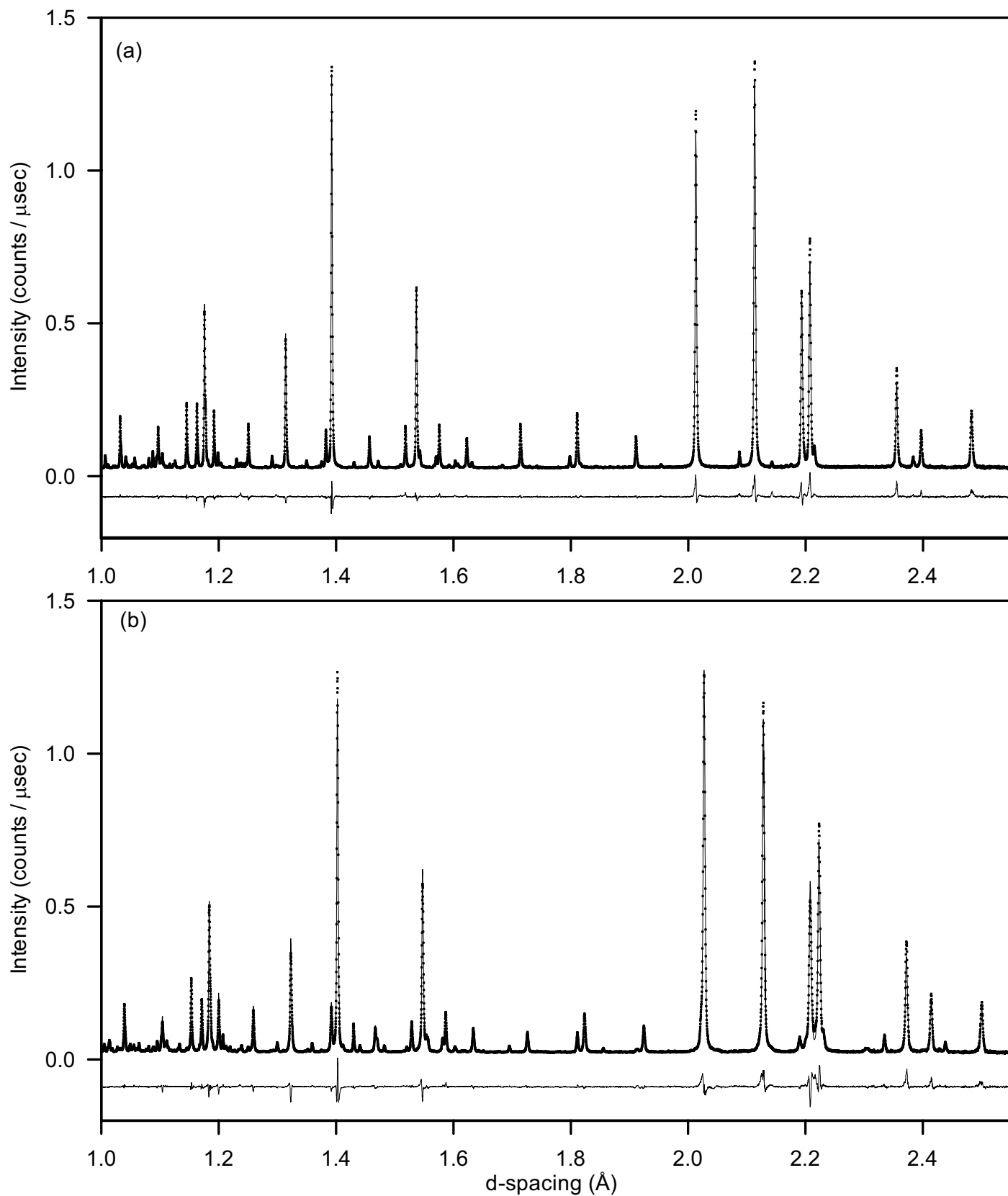


Figure 4 Doyle et al. 2013

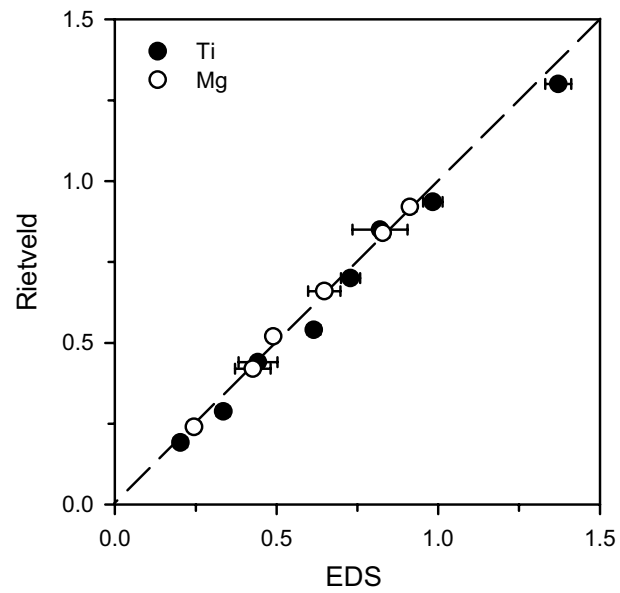


Figure 5 Doyle et al. 2013

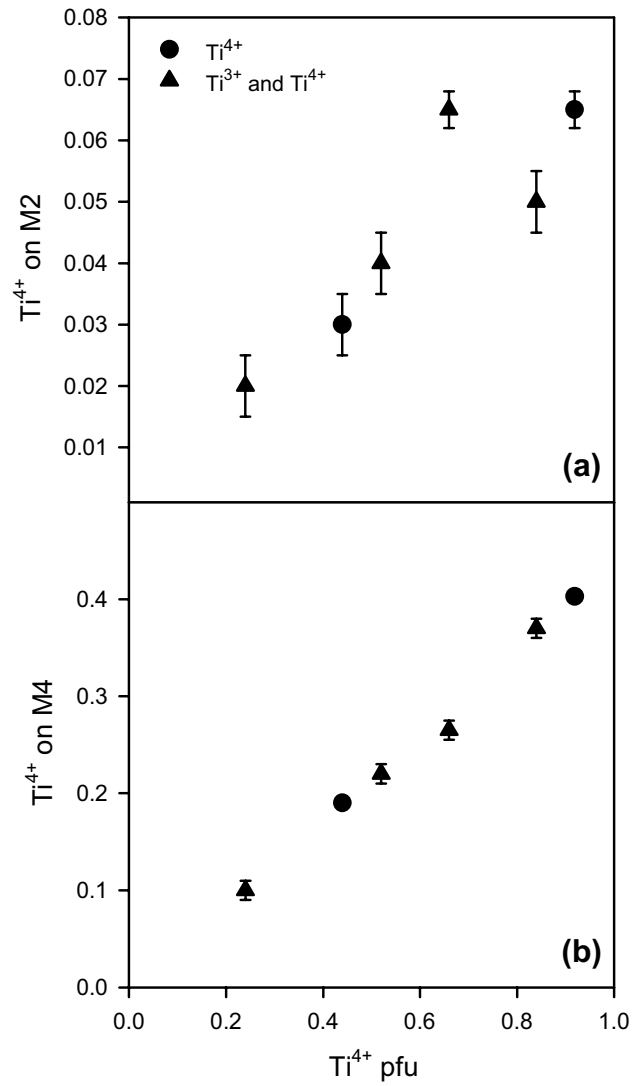


Figure 6 Doyle et al. 2013

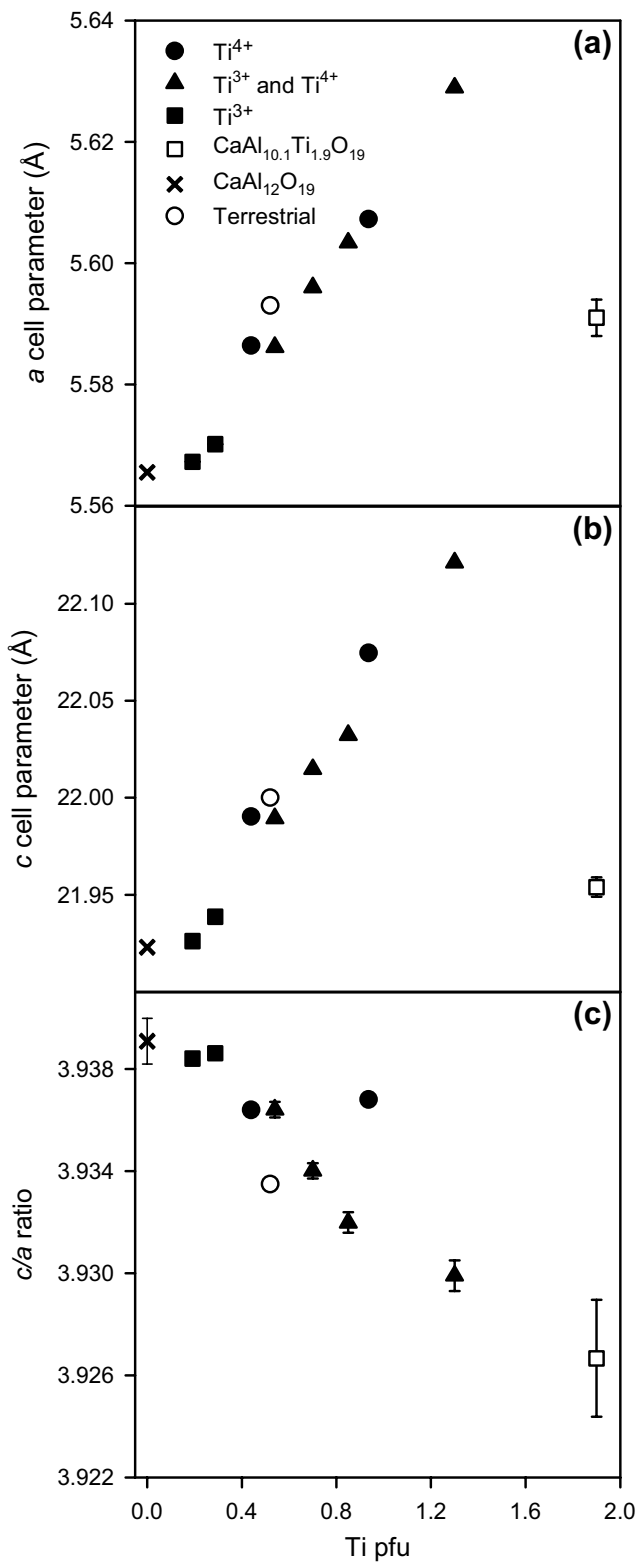


Figure 7 Doyle et al. 2013

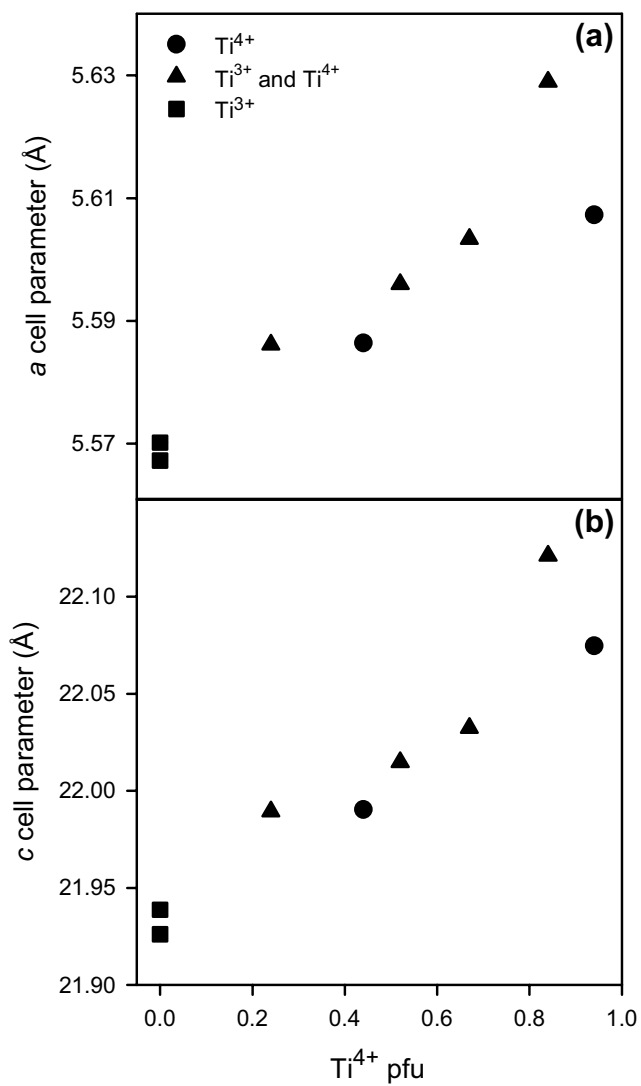


Figure 8 Doyle et al. 2013

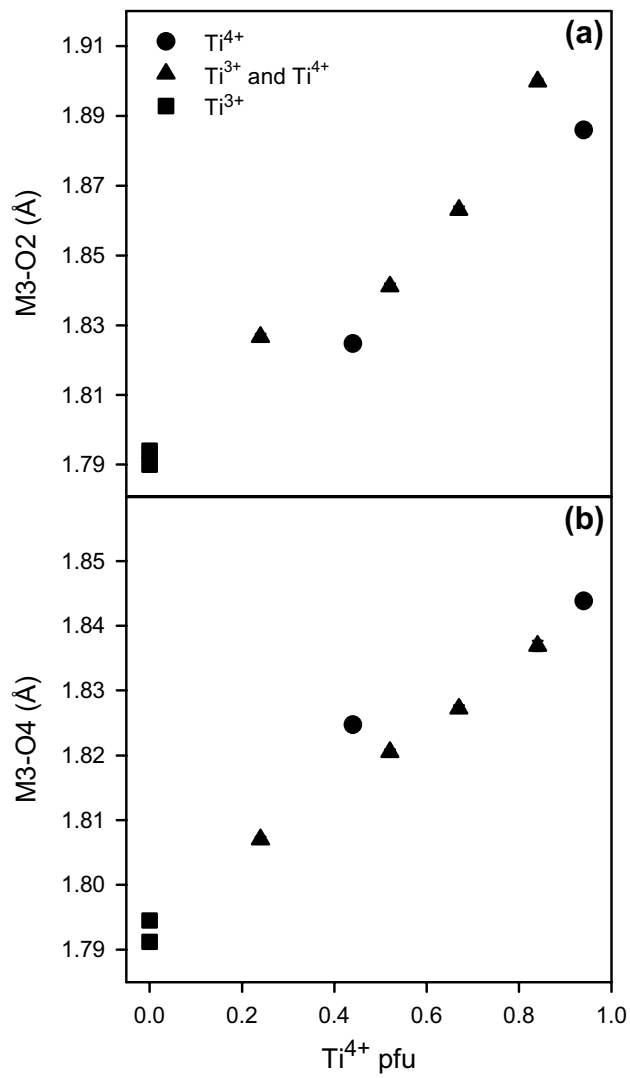
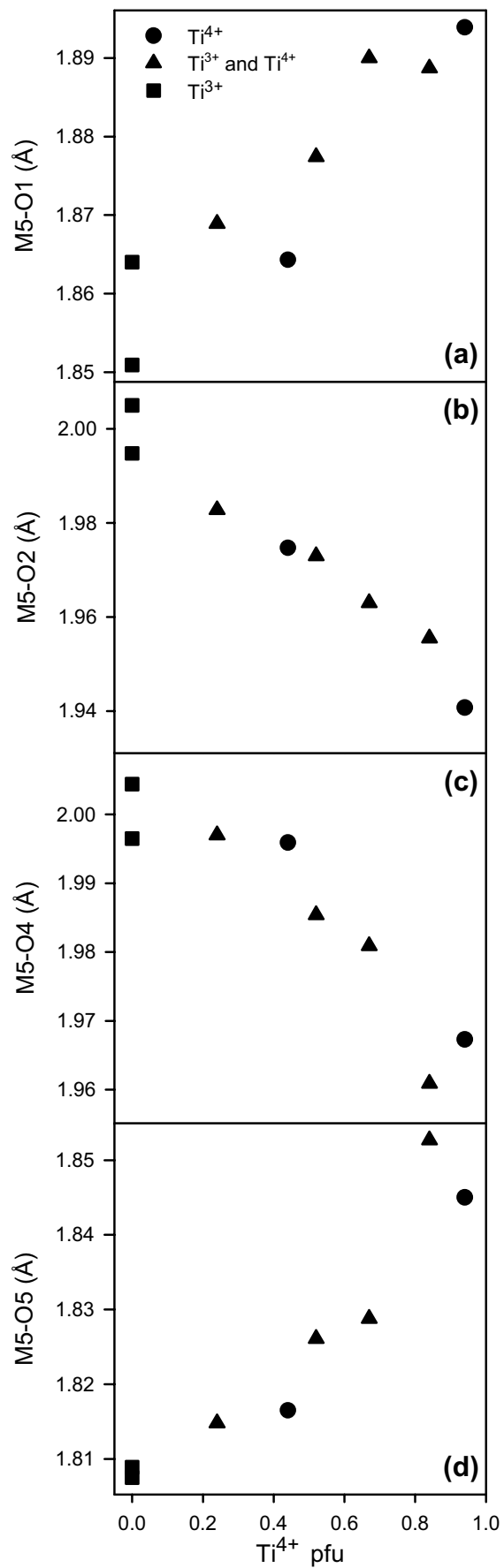


Figure 9 Doyle et al. 2013



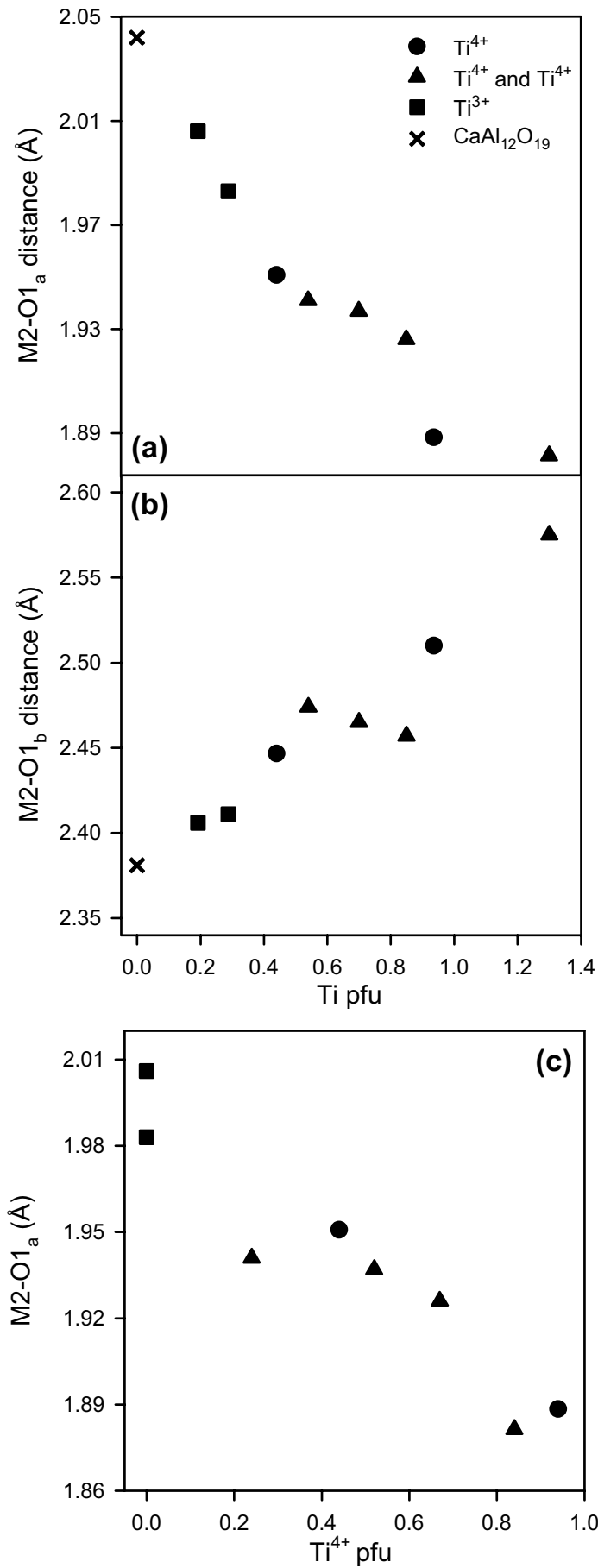


Figure 11 Doyle et al. 2013

